

PROBING THE IONIZATION STATES OF POLYCYCLIC AROMATIC HYDROCARBONS VIA THE 15–20 μm EMISSION BANDS

M. J. SHANNON¹, D. J. STOCK¹, AND E. PEETERS^{1,2}

¹ Department of Physics and Astronomy, University of Western Ontario, London, ON, N6A 3K7, Canada; mshann3@uwo.ca

² SETI Institute, 189 Bernardo Avenue, Suite 100, Mountain View, CA 94043, USA

Received 2015 June 28; accepted 2015 August 19; published 2015 October 1

ABSTRACT

We report new correlations between ratios of band intensities of the 15–20 μm emission bands of polycyclic aromatic hydrocarbons (PAHs) in a sample of 57 sources observed with the *Spitzer*/Infrared Spectrograph. This sample includes Large Magellanic Cloud point sources from the SAGE-Spec survey, nearby galaxies from the *Spitzer* Infrared Nearby Galaxies Survey survey, two Galactic interstellar medium cirrus sources, and the spectral maps of the Galactic reflection nebulae NGC 2023 and NGC 7023. We find that the 16.4, 17.4, and 17.8 μm band intensities are inter-correlated in all environments. In NGC 2023 and NGC 7023 these bands also correlate with the 11.0 and 12.7 μm band intensities. The 15.8 μm band correlates only with the 15–18 μm plateau and the 11.2 μm emission. We examine the spatial morphology of these bands and introduce radial cuts. We find that these bands can be spatially organized into three sets: the 12.7, 16.4, and 17.8 μm bands; the 11.2, 15.8 μm bands and the 15–18 μm plateau; and the 11.0 and 17.4 μm bands. We also find that the spatial distribution of the 12.7, 16.4, and 17.8 μm bands can be reconstructed by averaging the spatial distributions of the cationic 11.0 μm and neutral 11.2 μm bands. We conclude that the 17.4 μm band is dominated by cations, the 15.8 μm band by neutral species, and the 12.7, 16.4, and 17.8 μm bands by a combination of the two. These results highlight the importance of PAH ionization for spatially differentiating sub-populations by their 15–20 μm emission variability.

Key words: astrochemistry – infrared: ISM – ISM: lines and bands – ISM: molecules – molecular data – techniques: spectroscopic

1. INTRODUCTION

Polycyclic aromatic hydrocarbons (PAHs) are the most common polyatomic molecules in the universe (Tielens 2013) and are thought to produce prominent infrared emission bands at, e.g., 3.3, 6.2, 7.7, 8.6, 11.2, and 12.7 μm . These emission bands are seen in many different environments, including H II regions, reflection nebulae (RNe), planetary nebulae (PNe), and the diffuse interstellar medium (ISM). They are attributed to infrared (IR)-active vibrational modes, generally stretching or bending modes of C–C and/or C–H bonds. Bending modes of the carbon skeleton, denoted as C–C–C modes, produce weaker but identifiable emission features at 15.8, 16.4, 17.4, and 17.8 μm , typically perched atop a broad 17 μm plateau (e.g., Moutou et al. 2000; Van Kerckhoven et al. 2000; Van Kerckhoven 2002).

PAH emission bands can be separated into three categories. The 3–15 μm bands arise from nearest-neighbor vibrations, such as the 3.3 μm C–H stretch or the 8.6 μm in-plane C–H bend. These nearest-neighbor vibrations are common to all PAHs, and their collective emission features at similar wavelengths leads to blended emission. As a result, the emission intensities are high and they are readily observed in astronomical environments. In contrast, vibrations of the entire molecule (typically occurring at >20 μm , such as “drumhead” modes) are extremely molecule-dependent (e.g., Van Kerckhoven et al. 2000; Boersma et al. 2010, 2011; Ricca et al. 2010). The intensities of these bands are very low and they are difficult to detect; in fact, none have, to date, been identified in space. The 15–20 μm bands however represent an intermediate between the strong 3–15 μm bands and the rich but weak 20+ μm bands; they arise from vibrational modes involving a subset of the molecule (e.g., Van Kerckhoven et al. 2000; Peeters et al. 2004; Boersma et al. 2010). They are generally

thought to arise in PAHs with ~ 50 –200 carbon atoms (Boersma et al. 2010). The plateaus upon which the PAH bands sit are thought to arise from emission by large PAHs or PAH clusters (e.g., Allamandola et al. 1989; Tielens 2008).

The 3–15 μm bands are known to have a series of correlations between the intensities of specific bands, typically attributed to common properties (primarily ionization state). The 15–20 μm PAH bands however have thus far not exhibited any correlations among themselves (e.g., Smith et al. 2007b; Boersma et al. 2010; Ricca et al. 2010; Peeters et al. 2012, hereafter referred to as Paper I), though there are results showing the 16.4 μm band correlates with the 6.2 and 12.7 μm bands (Boersma et al. 2010, Paper I). Previous studies have had limited sample sizes of moderate quality or focused on single objects. Here we investigate correlations in a large sample of objects to examine the behavior of the 15–20 μm bands, and their relationship to the 3–15 μm emission features. The paper is organized as follows: the observations and data reduction are presented in Section 2. The methods used to analyze the spectra are summarized in Section 3. Results, including correlation plots and spatial maps, are presented in Section 4. We interpret these results in Section 5 and summarize our findings in Section 6.

2. OBSERVATIONS AND DATA REDUCTION

2.1. Target Selection

We obtained spectra of a variety of objects from the SAGE-Spectroscopy (SAGE-Spec) *Spitzer* legacy program (Kemper et al. 2010) and sources from the *Spitzer* Infrared Nearby Galaxies Survey (SINGS, Kennicutt et al. 2003). We chose sources displaying clear PAH emission in the 15–20 μm region. Such emission can be identified by a wide 17 μm

Table 1
Sample

Object	Type	Resolv. ^a	SSID ^b	AOR key	Extent ^c (")	R.A. [J2000]	Decl. [J2000]
HD 269211	H II? ^d	Integ.	4250	19151360	9.7	05 12 30.26	-70 24 21.75
HD 32364	H II? ^d	Integ.	4122	19150592	11.2	04 57 14.28	-68 26 30.55
IRAS 05192-6824	UCH II ^e	Integ.	4313	19011584	6.1	05 19 06.84	-68 21 36.41
IRSX 104	H II	Integ.	104	22425088	...	05 24 13.30	-68 29 58.98
IRSX 4087	H II	Integ.	4087	11239168	5.3	04 55 06.47	-69 17 08.30
IRSX 4713	YSO ^f	Integ.	4713	16943616	6.3	05 40 12.02	-70 10 05.83
IRSX 4729	YSO ^f	Integ.	4729	16943616	5.9	05 40 46.83	-70 11 22.73
IRSX 4755	YSO ^f	Integ.	4755	11239424	7.0	05 43 19.62	-69 26 27.68
MSX LMC 1306	H II	Integ.	4059	10958592	6.5	04 52 58.80	-68 02 56.77
MSX LMC 217	H II	Integ.	4263	10962176	5.9	05 13 24.68	-69 10 48.12
MSX LMC 559	H II	Integ.	4419	10963712	...	05 25 49.23	-66 15 08.50
MSX LMC 764	H II	Integ.	4538	10967040	7.6	05 32 52.62	-69 46 22.84
MSX LMC 836	H II	Integ.	4527	10966528	6.4	05 32 31.95	-66 27 15.15
MSX LMC 889	H II	Integ.	4621	10968576	6.7	05 38 31.64	-69 02 14.92
MSX LMC 934	H II	Integ.	4652	10969088	13.4	05 39 15.83	-69 30 38.39
N159-P2	YSO	Integ.	4665	12548352	10.8	05 39 41.88	-69 46 11.94
NGC 7023	RN	Extend.	...	3871232	...	21 01 32.50	+68 10 18.0
Cirrus1b	ISM	Extend.	...	4120832	...	17 32 53.80	-33 10 01.4
Cirrus3	ISM	Extend.	...	4119296	...	16 03 38.70	-52 18 01.7

Notes. Additional sources (not listed) are from Smith et al. (2007b), Boersma et al. (2010), and Peeters et al. (2012).

^a Whether the source is resolved or not (i.e., integrated spectrum or extended); integrated sources are from Surveying the Agents of Galaxy Evolution Spectroscopy program (SAGE-Spec; Kemper et al. 2010), data release 3.

^b SAGE-Spec ID number.

^c Point sources are those with no extent listed.

^d Object type uncertain in literature.

^e Ultra-compact H II region (Beasley et al. 1996).

^f Classification from P. M. Woods et al. 2015, (in preparation).

complex (or plateau) and narrower features at 15.8, 16.4, 17.4 and 17.8 μm . Sources more extended than 13''5 in the SAGE-Spec sample were excluded, as this corresponds to the approximate size of the SL aperture at 11.2 μm (which is used for normalization when comparing band intensity ratios). Only sources with a 3σ detection of their 15–20 μm emission components (or a subset) are included. We also applied this measurement criterion to the “MIR” (5–15 μm) PAH bands. Fifty-seven sources were identified as meeting these selection criteria, including two ISM cirrus sources. The sources in our sample are presented in Table 1. We also analyze a high-resolution spectral map of the RN NGC 7023 (Figure 1, previously analyzed by Rosenberg et al. 2011; Berné & Tielens 2012; Boersma et al. 2013, 2014b, 2015). We compare our results to that of NGC 2023 (Paper I and E. Peeters et al. 2015, in preparation, hereafter referred to as Paper II). The 15–20 μm measurements of Boersma et al. (2010), comprising 15 sources, are also included for comparison. Our total sample includes carbon-rich evolved stars, young stellar objects and H II regions in the Large Magellanic Cloud, nearby galaxies, Galactic RNe, and other ISM sources.

2.2. Observations

The spectra we analyze were acquired with the Infrared Spectrograph (IRS; Houck et al. 2004) on board the *Spitzer Space Telescope* (Werner et al. 2004). The IRS instrument provides high- and low-resolution spectroscopy in the mid-IR regime (5–40 μm). Low-resolution spectra ($R \sim 60$ –130) were obtained with the Short-low (SL) and Long-low (LL) modules, which provide coverage from 5–14 μm and 15–40 μm , respectively. We also analyze a high-resolution ($R \sim 600$)

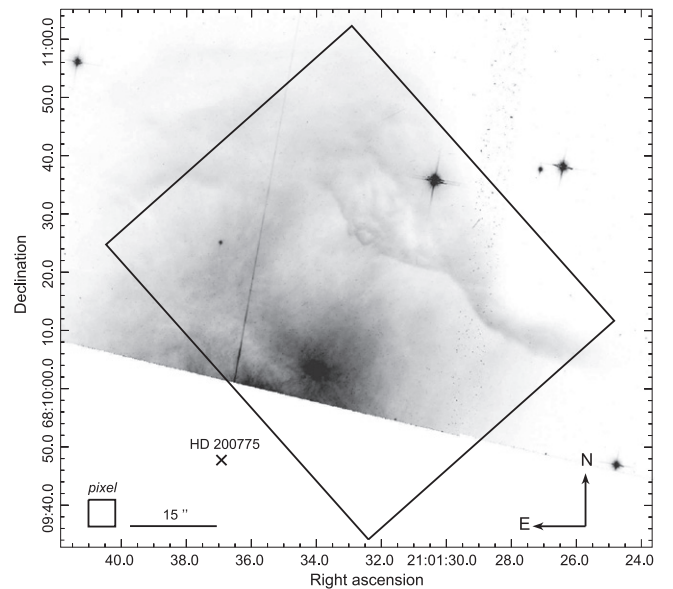


Figure 1. *Hubble Space Telescope* image of NGC 7023, with the *Spitzer*/IRS SH field of view outlined by the black box. This image is composed from four filters: wide-band filters at 475 and 625 nm, a long-pass filter at 850 nm, and a narrow-band filter at 658 nm. The exciting star, HD 200775, a B2.5 Ve star (Finkenzeller 1985), is indicated by the black cross toward the lower left.

spectral map of NGC 7023 and 2 ISM objects acquired with the IRS/Short-high (SH) module, covering the wavelength range 9.9–19.5 μm . These SH data were obtained from the NASA/IPAC *Spitzer* Heritage Archive³ (AORkey: 3871232, PI:

³ <http://sha.ipac.caltech.edu/applications/Spitzer/SHA/>

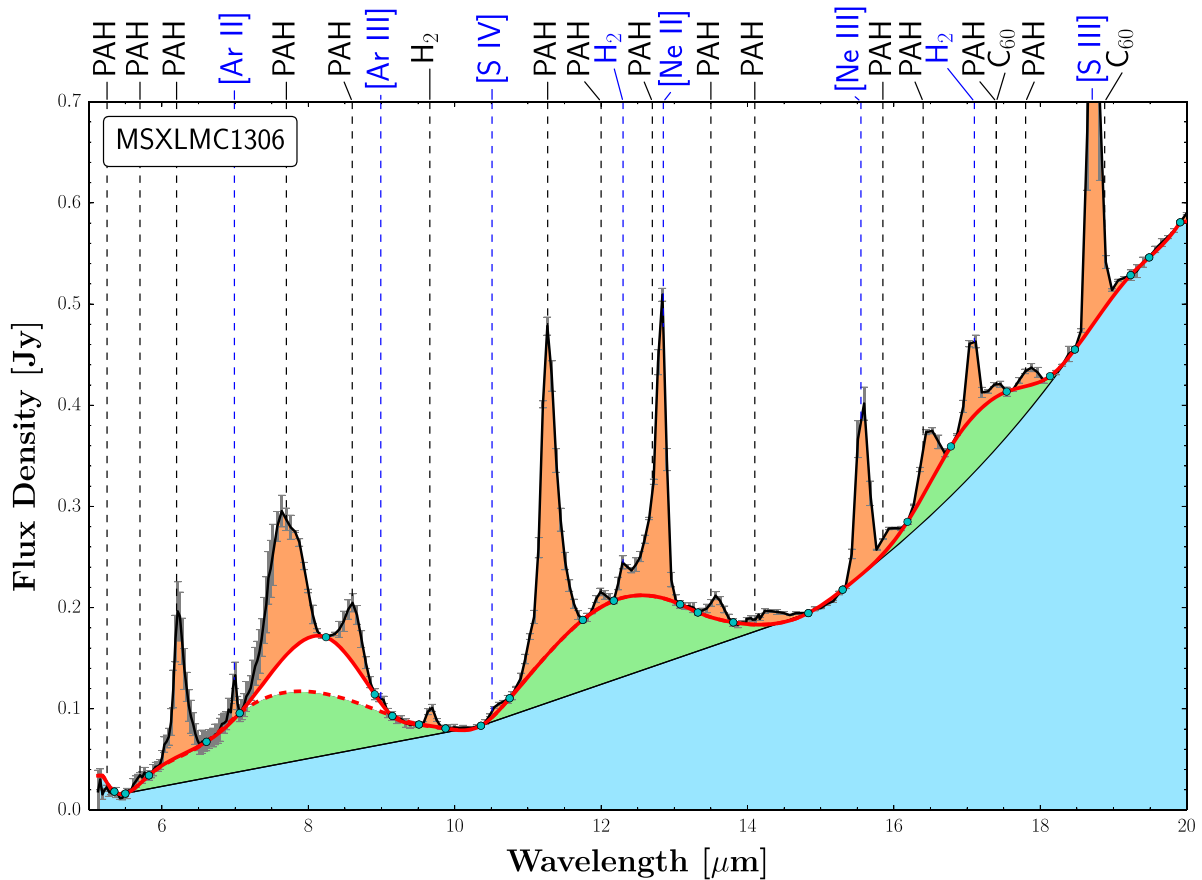


Figure 2. Typical IRS low-resolution spectrum from the SAGE-Spec sample is shown, that of LMC H II region MSX 1306. Prominent PAH features and atomic/molecular emission lines are visible (see labels at top). A local continuum is identified with a spline fit (red line). The continuum in the 5–10 μm range can be fit with or without a continuum point between the 7.7 and 8.6 μm features (see dashed red line). Three plateaus are identified underneath the PAH emission bands (green shaded region).

Giovanni Fazio). Previous studies that have examined these data are those of Sellgren et al. (2007), Rosenberg et al. (2011), Boersma et al. (2013, 2014b, 2015).

2.3. Reduction

The SAGE-Spec data included in this study were obtained in reduced form. The project and the data reduction process are described in detail by Kemper et al. (2010); we briefly review the reduction steps here. The *Spitzer* Science Center⁴ (SSC) data-reduction pipeline (version S18.7) was used to produce flat-field corrected images. Background subtraction was completed using on- and off-source nod positions. Rogue pixels were removed and replaced using the `imclean` algorithm, part of `irsclean`, provided by the SSC. Spectra were extracted using the SSC pipeline modules `profile`, `ridge`, and `extract`. Extracted spectra were coadded to produce one spectrum per nod position, per instrument module. The products were then calibrated and stitched together to produce the final spectra.

The SINGS data were also provided in reduced form by Smith et al. (2007b). These data were processed with IRS pipeline version S14 and reduced with the `CUBISM` tool (Smith et al. 2007a), including scaling and stitching of spectral segments to construct the final low-resolution spectra.

The SH maps of NGC 7023, Cirrus 1b and Cirrus 3 were reduced in a similar manner to that of NGC 2023, which was described in Paper I. The raw data were processed by the SSC, using pipeline version S18.7. The reduction process was completed using `CUBISM` (Smith et al. 2007a), including co-addition and bad pixel cleaning. The extraction for NGC 7023 was accomplished by stepping a 2×2 -pixel aperture across the map.

3. ANALYSIS

3.1. Spectral Inventory

A typical IRS low-resolution spectrum is shown in Figure 2, represented by the H II region MSX LMC 1306. A rising mid-to-far-IR dust continuum is common in many objects in the sample. There are also several atomic emission lines frequently present, including [Ar II] 6.99 μm , [Ar III] 8.99 μm , [S IV] 10.51 μm , [Ne II] 12.81 μm , [Ne III] 15.56 μm , and [S III] 18.71 μm . We frequently observe the S(3) 9.7 μm , S(2) 12.3 μm and S(1) 17.0 μm rotational lines of H_2 , and occasionally C_{60} fullerene emission at 17.4 and 18.9 μm (Cami et al. 2010; Sellgren et al. 2010). The PAH features at 6.2, 7.7, 8.6, 11.2, 12.7, 15.8, 16.4, 17.4, and 17.8 μm are visible in all sources. Note that the 17.4 μm band arises from both PAH and C_{60} emission (Sellgren et al. 2010). In addition to the aforementioned PAH emission bands, there are several weaker PAH bands visible at 5.25, 5.75, 6.0, 11.0, 12.0, 13.5, and

⁴ <http://ssc.spitzer.caltech.edu>

14.2 μm . Strong emission plateaus from 5–10 μm , 10–15 μm , and 15–18 μm are observed. Additionally, some spectra display a strong silicon carbide feature at 11 μm (Treffers & Cohen 1974; Bernard-Salas et al. 2009).

3.2. Spectral Decomposition

A local spline continuum is fit to each spectrum to isolate the PAH emission features (Figure 2), a method that has been used in several previous studies (e.g., Hony et al. 2001; Peeters et al. 2002; Bernard-Salas et al. 2009; Boersma et al. 2010; Stock et al. 2013, 2014). Spline anchor points are chosen to be adjacent to emission features, and are allowed to move within a predefined window. When necessary, smoothing and/or a process that locates local minima are used to improve anchor positions. In addition to the local continuum, a global continuum is defined. This continuum underscores the emission plateaus at 5–10 μm , 10–15 μm , and 15–18 μm . The 7.7 and 8.6 μm features can be drawn with or without a spline anchor point between them, depending on the decomposition. Here, we use such an anchor point near 8.2 μm . The molecular hydrogen and atomic emission lines will be dealt with separately and are discussed in Section 3.3.

Other methods for measuring the PAH bands are possible and are considered in the literature. These include fitting Drude profiles to the individual components (the PAHFIT tool; Smith et al. 2007b) or Lorentzian profiles (Boulanger et al. 1998; Galliano et al. 2008). It has been shown that the decomposition method chosen affects the measured band intensities, but it does not affect the trends found in the correlations of band intensity ratios (Smith et al. 2007b; Galliano et al. 2008). The spline decomposition method is chosen here for comparison with previous 15–20 μm PAH studies (Paper I, Paper II, Boersma et al. 2010).

3.3. Measurement Methods

The plateaus are measured by direct integration between the global continuum and local continuum (see Figure 2). After subtracting the local continuum, PAH band fluxes in the 5–15 μm range are measured by direct integration, except for the 6.0, 11.0, and 12.7 μm bands. The 6.0 and 11.0 μm bands are blended with the 6.2 and 11.2 μm bands in low-resolution spectra, respectively. Therefore, Gaussians are used to separate these subfeatures and determine their fluxes (see Paper II for details). Special care is required when measuring the 12.7 μm PAH feature, as it blends with the 12.8 μm [Ne II] line and the 12.3 μm H₂ line (when present). We separate these components by scaling the average 12.7 μm PAH band profile (from Hony et al. 2001) to fit the data between 12.45 and 12.6 μm , where only PAH emission is expected (Figure 3). After subtracting the scaled PAH profile, the remaining lines are fit with Gaussians. This method is identical to the decomposition described by Stock et al. (2014), though we use the range 12.45–12.6 μm instead of 12.4–12.6 μm . This is because the 12.3 μm H₂ line is strong enough in some of our spectra to produce non-negligible (albeit minor) emission redward of 12.4 μm . We test for systematic effects in this decomposition by constructing an artificial spectrum. It is composed of the average 12.7 μm PAH band profile from Hony et al. (2001) plus two Gaussians, for the 12.3 H₂ line and the 12.8 [Ne II] line, and a variable amount of noise. We find that the derived PAH flux corresponds to the input artificial PAH flux within

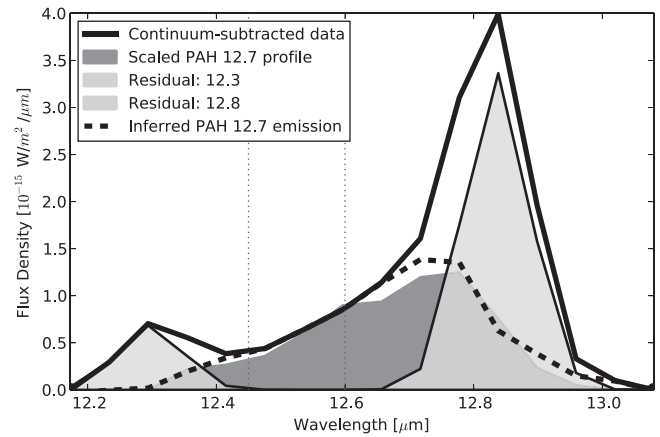


Figure 3. Example decomposition of the 12.7 μm complex. The continuum-subtracted spectrum (solid line) is fit with the scaled mean 12.7 μm PAH band profile (dark gray shading), as found by Hony et al. (2001). The fit is performed between 12.45 and 12.65 μm (denoted by the dotted vertical lines). The fitted PAH profile (dark gray shading) can then be subtracted from the spectrum, leaving a remainder of the 12.3 μm H₂ emission line and the 12.8 μm [Ne II] line (light gray shading). Returning to the original continuum-subtracted data, subtracting the two atomic lines then leaves only the inferred PAH 12.7 μm emission (dashed line).

2%–3% when the integrated strength of the [Ne II] line is less than 10 times that of the 12.7 PAH band. This is true for all our sources. The 12.3 μm H₂ line in our sample does not influence the derived PAH flux when decomposed this way.

The 15–20 μm PAH bands and the atomic/molecular lines are also measured through Gaussian decomposition. The 16.4 μm band is slightly asymmetric, while the other 15–20 μm PAH bands are symmetric (Paper I). There is frequent blending between the 15.55 μm [Ne III] line and the 15.8 μm PAH feature, as well as between the 17.1 μm H₂ line and the 17.4 μm PAH band in low-resolution spectra. Emission by the fullerene C₆₀ is known to be present at 17.4 and 18.9 μm in some objects (Cami et al. 2010; Sellgren et al. 2010). The 17.4 μm C₆₀ emission is approximately half of the intensity of the 18.9 μm band (estimated to be ~ 0.4 in Sellgren et al. 2010, ~ 0.6 in Cami et al. 2010 and ~ 0.5 in Bernard-Salas et al. 2012; we adopt 0.5). The 18.9 μm band is observed in some of our spectra, typically blended to some degree with the 18.7 [S III] line in low-resolution spectra. We examine the presence of C₆₀ emission by fitting the data with the model of C₆₀ emission from TC1 (Cami et al. 2010) and an appropriate Gaussian for the [S III] 18.71 μm line. In the sample of integrated sources, we detect C₆₀ emission in four objects: IRSX 4755 (with associated signal-to-noise ratio, or S/N, of 3.4), IRSX 4087 (5.6), HD 32364 (5.5), and HD 269211 (5.9). We correct our measured 17.4 μm band flux by subtracting the expected 17.4 μm C₆₀ component when the 18.9 μm C₆₀ band is present. The residual flux, if significant, is then attributed to the 17.4 μm PAH band.

The measured PAH and C₆₀ fluxes of the SAGE-Spec sources and the two cirrus sources are presented in Table 2. The fluxes of the SINGS sources are shown in Table 3.

4. RESULTS

We examine correlations between the 15–20 μm bands and the spatial distribution of the PAH emission in the extended RNe. NGC 2023S and NGC 2023N refer to the south and north

Table 2
PAH Emission Band Fluxes: SAGE and ISM Sources

Object	6.2 μm	7.7 μm	8.6 μm	11.2 μm	12.7 μm	15.8 μm	16.4 μm	17.4 μm	17.8 μm	Plateau	18.9 μm C ₆₀
HD 269211	3.64 (1.14)	13.09 (2.02)	22.66 (1.51)	...	1.77 (0.11)	0.42 (0.11)	0.56 (0.10)	8.81 (0.88)	1.07 (0.18)
HD 32364	24.65 (1.68)	23.01 (1.04)	...	2.02 (0.12)	0.42 (0.08)	0.79 (0.14)	16.91 (1.69)	1.43 (0.26)
IRAS 05192-6824	14.10 (0.77)	28.35 (1.85)	4.44 (0.98)	14.75 (1.70)	14.35 (1.56)	...	1.54 (0.19)	7.99 (0.80)	...
IRSX 104	8.33 (1.53)	10.40 (1.15)	...	6.45 (0.71)	3.28 (0.75)	0.44 (0.12)	0.72 (0.14)
IRSX 4087	9.41 (1.15)	14.48 (1.34)	3.50 (0.75)	10.60 (0.67)	10.07 (0.74)	0.63 (0.13)	1.13 (0.15)	...	0.48 (0.12)	5.27 (0.53)	1.62 (0.29)
IRSX 4713	5.76 (0.64)	8.47 (0.60)	2.05 (0.20)	5.43 (0.18)	1.48 (0.18)	...	0.41 (0.10)
IRSX 4729	6.95 (1.00)	10.65 (1.23)	2.17 (0.64)	5.82 (0.57)	1.92 (0.29)	...	0.41 (0.08)	2.04 (0.20)	...
IRSX 4755	18.30 (2.66)	23.74 (3.48)	5.13 (0.94)	10.38 (1.17)	6.02 (0.91)	...	0.82 (0.11)	0.34 (0.10)
MSX LMC 1306	21.60 (5.09)	38.72 (5.16)	6.76 (1.38)	20.59 (1.33)	12.46 (0.86)	0.48 (0.10)	1.64 (0.10)	...	0.46 (0.09)	8.48 (0.85)	...
MSX LMC 217	27.09 (4.94)	52.02 (4.33)	7.27 (2.00)	27.14 (1.43)	24.50 (1.25)	...	2.30 (0.25)	11.70 (1.17)	...
MSX LMC 222	3.10 (0.33)	6.97 (0.31)	0.82 (0.11)
MSX LMC 559	31.00 (1.43)	56.55 (1.39)	7.92 (1.01)	18.46 (0.87)	17.97 (1.30)	...	1.86 (0.61)
MSX LMC 764	...	76.81 (13.82)	...	39.66 (5.74)	33.30 (3.61)	1.85 (0.33)	4.40 (0.18)	0.96 (0.11)	2.09 (0.31)
MSX LMC 836	22.14 (0.67)	34.98 (1.29)	5.80 (0.52)	19.88 (0.57)	9.74 (0.41)	...	1.28 (0.12)	...	0.52 (0.13)	7.88 (0.79)	...
MSX LMC 889	61.10 (7.74)	154.46 (6.41)	20.51 (4.29)	70.84 (5.38)	80.30 (3.13)	...	8.00 (0.17)	1.47 (0.28)	2.79 (0.34)	36.50 (3.65)	...
MSX LMC 934	50.93 (1.71)	52.89 (2.34)	...	4.88 (0.54)	0.97 (0.32)	1.94 (0.47)	23.38 (2.34)	...
N159-P2	32.70 (0.85)	21.82 (0.99)	...	5.01 (0.80)	...	1.93 (0.63)
Cirrus1b	52.84 (1.08)	33.84 (0.87)	1.60 (0.29)	3.60 (0.48)	1.37 (0.28)	1.30 (0.32)
Cirrus3	49.67 (0.94)	27.65 (0.61)	1.91 (0.18)	3.38 (0.18)	1.22 (0.23)	0.95 (0.17)

Note. In units of 10^{-16} W m⁻², except the two extended cirrus sources, which are in units of 10^{-2} W m⁻² sr⁻¹. Uncertainties are given in parentheses.

Table 3
PAH Emission Band Fluxes: SINGS Sources

Object	6.2 μm	7.7 μm	8.6 μm	11.2 μm	12.7 μm	15.8 μm	16.4 μm	17.4 μm	17.8 μm	Plateau
MRK 33	7.82 (1.26)	13.88 (1.49)	3.33 (0.39)	5.43 (0.30)	3.72 (0.29)	...	0.45 (0.09)	0.16 (0.04)	0.16 (0.05)	...
NGC 0337	...	17.62 (1.62)	3.58 (0.45)	7.84 (0.38)	3.83 (0.30)	...	0.56 (0.10)	3.47 (0.35)
NGC 0628	3.48 (0.51)	0.25 (0.05)
NGC 0855	3.50 (0.90)	0.31 (0.08)
NGC 0925	4.72 (0.92)	0.27 (0.06)
NGC 1097	73.72 (1.36)	157.03 (1.58)	24.29 (0.47)	65.07 (0.42)	38.90 (0.38)	1.07 (0.22)	3.58 (0.42)	1.56 (0.45)	...	25.74 (2.57)
NGC 1482	100.70 (1.51)	230.20 (2.04)	31.10 (0.76)	74.11 (0.71)	4.36 (1.29)
NGC 1512	9.05 (1.48)	0.47 (0.08)	3.42 (0.34)
NGC 2403	7.51 (1.29)	10.42 (1.37)	...	5.13 (0.62)	0.43 (0.05)
NGC 2798	47.55 (0.90)	29.26 (0.84)	0.83 (0.23)	2.07 (0.35)	1.10 (0.30)
NGC 2976	4.56 (0.64)	0.38 (0.05)	1.83 (0.18)
NGC 3049	5.41 (0.75)	3.25 (0.68)	...	0.28 (0.06)
NGC 3184	8.38 (1.08)	5.47 (1.02)	...	0.31 (0.04)
NGC 3265	8.15 (0.75)	3.89 (0.74)	...	0.46 (0.11)
NGC 3351	16.01 (1.94)	53.97 (2.09)	5.30 (0.82)	17.63 (0.84)	11.64 (0.85)	...	1.04 (0.15)	12.92 (1.29)
NGC 3521	13.44 (1.50)	43.05 (1.72)	6.01 (0.59)	16.56 (0.52)	...	0.33 (0.07)	1.21 (0.10)	0.36 (0.08)	0.33 (0.10)	13.29 (1.33)
NGC 3621	15.28 (1.58)	12.12 (0.63)	4.96 (0.67)	...	0.74 (0.06)	0.21 (0.06)	...	4.64 (0.46)
NGC 3627	16.27 (1.86)	27.32 (2.04)	4.40 (0.71)	19.59 (0.86)	...	0.44 (0.08)	0.86 (0.12)	10.66 (1.07)
NGC 3773	4.12 (0.89)
NGC 3938	3.00(0.20)	1.48 (0.20)	...	0.18 (0.05)	2.18 (0.22)
NGC 4254	23.23 (1.35)	1.61 (0.16)	8.40 (0.84)
NGC 4321	33.00 (2.12)	69.04 (2.58)	10.03 (1.01)	27.13 (1.07)	14.83 (1.10)	...	1.26 (0.15)	0.54 (0.14)	...	11.56 (1.16)
NGC 4536	91.38 (2.19)	192.04 (2.54)	27.99 (0.79)	66.01 (0.70)	...	1.13 (0.36)	2.86 (0.55)	29.12 (2.91)
NGC 4559	5.29 (0.47)	2.84 (0.41)	...	0.36 (0.06)	0.12 (0.04)
NGC 4569	5.89 (1.16)	24.68 (1.24)	...	0.44 (0.09)	1.23 (0.09)	14.15 (1.41)
NGC 4579	4.76 (1.12)	0.40 (0.11)
NGC 4631	30.72 (0.55)	...	0.47 (0.13)	2.09 (0.20)
NGC 4736	34.32 (1.62)	40.69 (2.13)	9.73 (0.99)	48.69 (1.08)	...	0.89 (0.12)	2.03 (0.18)	0.47 (0.14)	0.51 (0.12)	16.99 (1.70)
NGC 4826	44.40 (2.21)	108.11 (2.58)	18.10 (1.32)	42.38 (1.44)	...	0.93 (0.11)	2.30 (0.18)	0.72 (0.16)	0.72 (0.10)	19.41 (1.94)
NGC 5033	19.75 (1.76)	36.88 (1.75)	6.15 (0.79)	17.27 (0.81)	8.47 (0.74)	...	0.91 (0.14)	0.33 (0.10)	0.29 (0.09)	9.01 (0.90)
NGC 5055	16.65 (1.42)	44.23 (1.76)	...	21.37 (0.81)	0.97 (0.10)	0.30 (0.08)	0.30 (0.06)	10.06 (1.01)
NGC 5194	27.32 (1.27)	56.63 (1.59)	10.35 (0.89)	29.35 (0.88)	...	0.48 (0.10)	1.28 (0.14)	0.43 (0.11)	0.34 (0.09)	12.83 (1.28)
NGC 5195	...	32.48 (2.59)	...	36.03 (1.28)	1.93 (0.46)	15.19 (1.52)
NGC 5713	36.36 (1.25)	75.25 (1.62)	11.23 (0.72)	29.04 (0.69)	1.78 (0.16)	12.49 (1.25)
NGC 5866	8.24 (0.86)	...	0.22 (0.05)	0.34 (0.07)
NGC 6946	90.92 (1.93)	189.33 (2.10)	29.22 (1.11)	61.51 (1.05)	4.34 (0.41)	33.86 (3.39)
NGC 7331	15.56 (1.26)	...	0.27 (0.08)	0.83 (0.08)	7.93 (0.79)
NGC 7552	81.57 (1.84)	173.99 (2.22)	26.90 (0.97)	71.78 (0.96)	47.74 (0.95)	...	4.79 (0.97)

Notes. In units of $10^{-14} \text{ W m}^{-2}$. Uncertainties are given in parentheses. No 3σ detections of $18.9 \mu\text{m}$ C_{60} emission were found for these data.

maps of NGC 2023, respectively (Papers I and II). Band fluxes in the correlation study are typically normalized to the $11.2 \mu\text{m}$ band. Normalization is required because PAH abundances and object distances will vary from source to source. Only band ratios with 3σ detections are included. The weighted Pearson correlation coefficients for all correlations are presented in Table 4.

4.1. Correlation Plots

4.1.1. The 16.4, 17.4 and 17.8 μm Bands

Correlation plots of the 16.4, 17.4, and 17.8 μm bands are presented in Figure 4. We address these in turn.

17.8 versus 16.4 μm . These band fluxes are the strongest correlated for the integrated sources (correlation coefficient

Table 4
Weighted Pearson Correlation Coefficients

Correlation	Integrated Sources	N7023 ^a	N2023N ^b	N2023S ^b
17.4 versus 16.4	0.67	0.80	0.57	0.45
17.8 versus 16.4	0.93	0.85	0.72	0.82
17.8 versus 17.4	0.63	0.53	0.97	0.47
16.4 versus 15.8	0.74	0.22	...	-0.28
17.4 versus 15.8	0.58	0.37	...	-0.14
17.8 versus 15.8	0.75	0.40	...	-0.08
15.8 versus 11.2	-0.28	0.38	...	0.89
Plat. versus 11.2	0.42	0.47	0.92	0.87
Plat. versus 15.8	0.28	0.46	...	0.88
12.7 versus 11.0	0.51	0.95	0.88	0.91
16.4 versus 11.0	0.36	0.92	0.92	0.95
17.4 versus 11.0	-0.14	0.84	0.69	0.51
17.8 versus 11.0	-0.26	0.87	0.89	0.81
16.4 versus 12.7	0.28 [0.68] ^c	0.89	0.88	0.92
17.4 versus 12.7	0.69	0.83	0.55	0.35
17.8 versus 12.7	0.23 [0.66] ^c	0.86	0.53	0.71

Notes.

^a See individual correlation plots for coefficients organized by region; regions defined in Figure 10.

^b See also Paper I, II.

^c H II regions alone.

$r = 0.93$). Some segregation by object type is observed: two evolved stars sit at the lowest ratios of 16.4/11.2 and 17.8/11.2 (0.030 and 0.010, respectively), galaxies slightly higher at (0.060, 0.015), and H II regions at the highest values (centered near 0.10, 0.035). The galaxies and H II regions each span a range covering roughly a factor of two on each axis. The 17.8 and 16.4 μm bands also correlate in the RNe. NGC 7023 has a correlation coefficient of $r = 0.85$ and spans nearly the same variation in 16.4/11.2 and 17.8/11.2 as the integrated sources. NGC 2023S has a correlation coefficient of $r = 0.82$ and has a line of best fit close to that of NGC 7023, despite spanning half the range in abscissa; NGC 2023N has a similar range and correlation coefficient ($r = 0.72$). Its line of best fit is closer to the fit for the integrated sources, but it should be noted it also has far fewer pixels than those contained in the NGC 7023 or NGC 2023S maps given the S/N criterion.

17.4 versus 16.4 μm . The 17.4 and 16.4 μm band fluxes are observed to correlate. NGC 7023 exhibits a correlation coefficient of $r = 0.80$, while NGC 2023S and 2023N have associated coefficients of $r = 0.45$ and $r = 0.57$, respectively. NGC 7023 and NGC 2023 have similar lines of best fit. The integrated sources however display a trend on a much steeper gradient, aside from two lone H II regions, and have a correlation coefficient of $r = 0.67$. The integrated sources and NGC 2023 generally span the same abscissa and ordinate ranges, but NGC 7023 is set to higher ratios of 16.4/11.2, with only modest overlap with NGC 2023 and the integrated sources. This correlation was previously observed by Berné & Tielens (2012).

17.8 versus 17.4 μm . The 17.8 and 17.4 μm bands also correlate. The integrated sources and NGC 7023 span similar

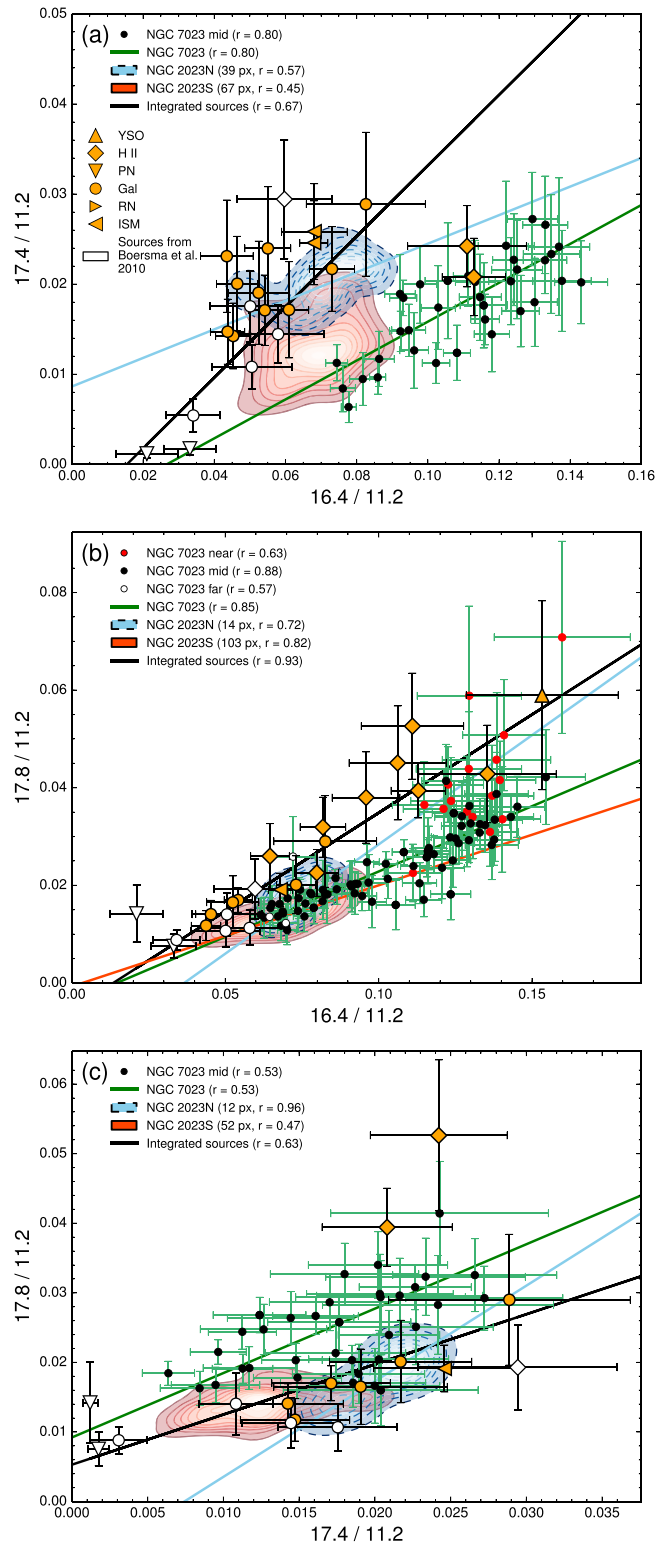


Figure 4. Correlation plots of flux ratios among the 16.4, 17.4, and 17.8 μm features. The filled blue and orange density contours represent the number densities of measurements of NGC 2023 north and south, respectively (Papers I and II). Each displays 10 linear contour levels, computed with a Gaussian kernel. The data points with green errorbars are from NGC 7023, separated into three regions (defined in Figure 10): data nearest to the exciting star (red dots); data from the center of the map, the peak PAH emission region (black dots); and data furthest from the exciting star (white dots). Each grouping is shown with an associated line of best fit when the correlation coefficient exceeds $r = 0.50$: integrated sources (black line), NGC 7023 (green line), NGC 2023N (blue line), NGC 2023S (orange line).

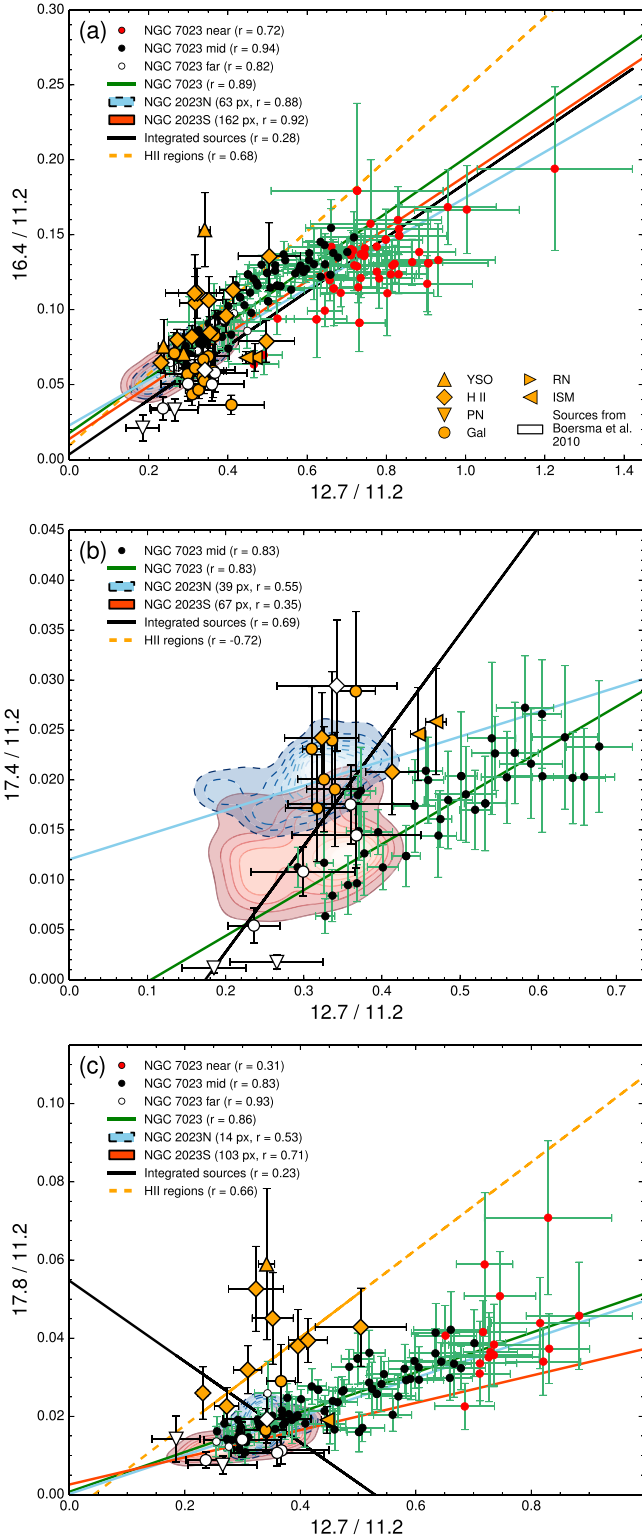


Figure 5. Correlation plots of the 16.4, 17.4, and 17.8 μm band fluxes vs. the 12.7 μm band flux, each normalized to the 11.2 μm band flux.

ranges in abscissa and ordinate values, with associated coefficients $r = 0.63$ and $r = 0.53$, respectively. NGC 2023 spans half the range of 17.8/11.2 in comparison, though a similar extent is observed in 17.4/11.2. NGC 2023S has correlation coefficient of $r = 0.47$ and NGC 2023N of $r = 0.97$, though the latter has far fewer data points included

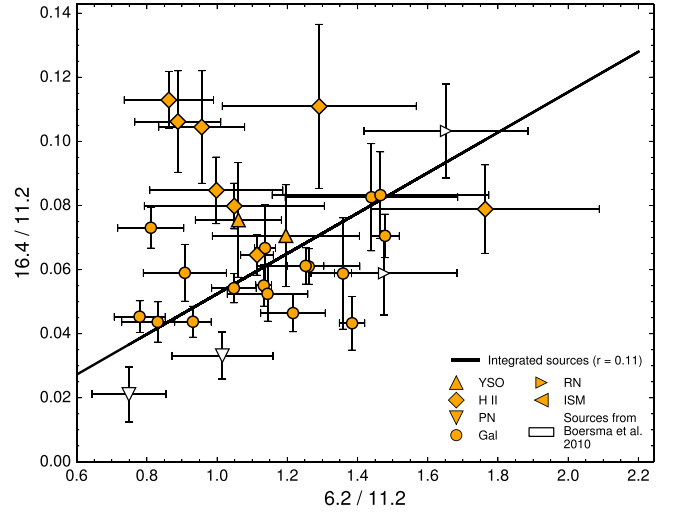


Figure 6. No linear relationship is observed between the 16.4 and 6.2 μm bands ($r = 0.11$); however, the lower-right quadrant is conspicuously devoid of sources, and our data span a small range of values (c.f. Boersma et al. 2014b).

(12 versus 52, respectively). The individual sources again fall upon a slightly different gradient, as they appear to be displaced toward higher 17.4/11.2 values. The outlying HII regions in this figure are also the outliers in the correlation plot of the 17.4 and 16.4 μm bands. Systematic problems may affect the 17.4 μm band measurement in our sample as its derived flux is dependent on an accurate measurement of the 18.9 μm C₆₀ band. When the latter cannot be observed (or reliably measured) it is possible that the derived 17.4 μm PAH band flux is overestimated, as the 17.4 μm C₆₀ contribution cannot be removed, if present. This issue is particularly prominent in low-resolution spectra, which comprise most of the integrated sources in this sample (apart from the two ISM cirrus sources), as the 18.9 μm C₆₀ band blends with the [S III] 18.71 μm line. The RNe were observed in high resolution and are less susceptible to this type of overestimation, which may explain why the gradients observed in the correlation plots involving the 17.4 μm band differ for integrated sources versus RNe (e.g., Figure 4).

Correlations with the 12.7 μm band. The 16.4, 17.4, and 17.8 μm bands are observed to correlate with the 12.7 μm band (Figure 5). NGC 7023 displays a high correlation coefficient ($r = 0.89$), though there is deviation from the linear fit in our data at high abscissa values. In our data, there is a cluster of data points at 12.7/11.2 = 0.75, 16.4/11.2 = 0.13, all of which originate in the third of the map nearest the exciting star in NGC 7023. Regardless, we find a strong correlation between these band ratios in NGC 7023, peaking in the middle portion of the map ($r = 0.94$; see Figure 10 for map region definitions). The gradient of the NGC 7023 data is consistent with those of NGC 2023 (both north and south). The integrated sources of this study show no trend as a whole, but they do tend to cluster about a position coincident with the center of the NGC 2023 data. The subset of HII regions alone however do display a correlation ($r = 0.68$). Since the 16.4, 17.4, and 17.8 μm bands correlate (Figure 4), it is not surprising that we find that the 17.4 and 17.8 μm bands correlate with the 12.7 μm band in RNe. We additionally observe that HII regions display a correlation between the 17.8 and 12.7 μm bands. Nothing can be determined about HII regions among the 17.4 and 12.7 μm bands as there are too few sources meeting

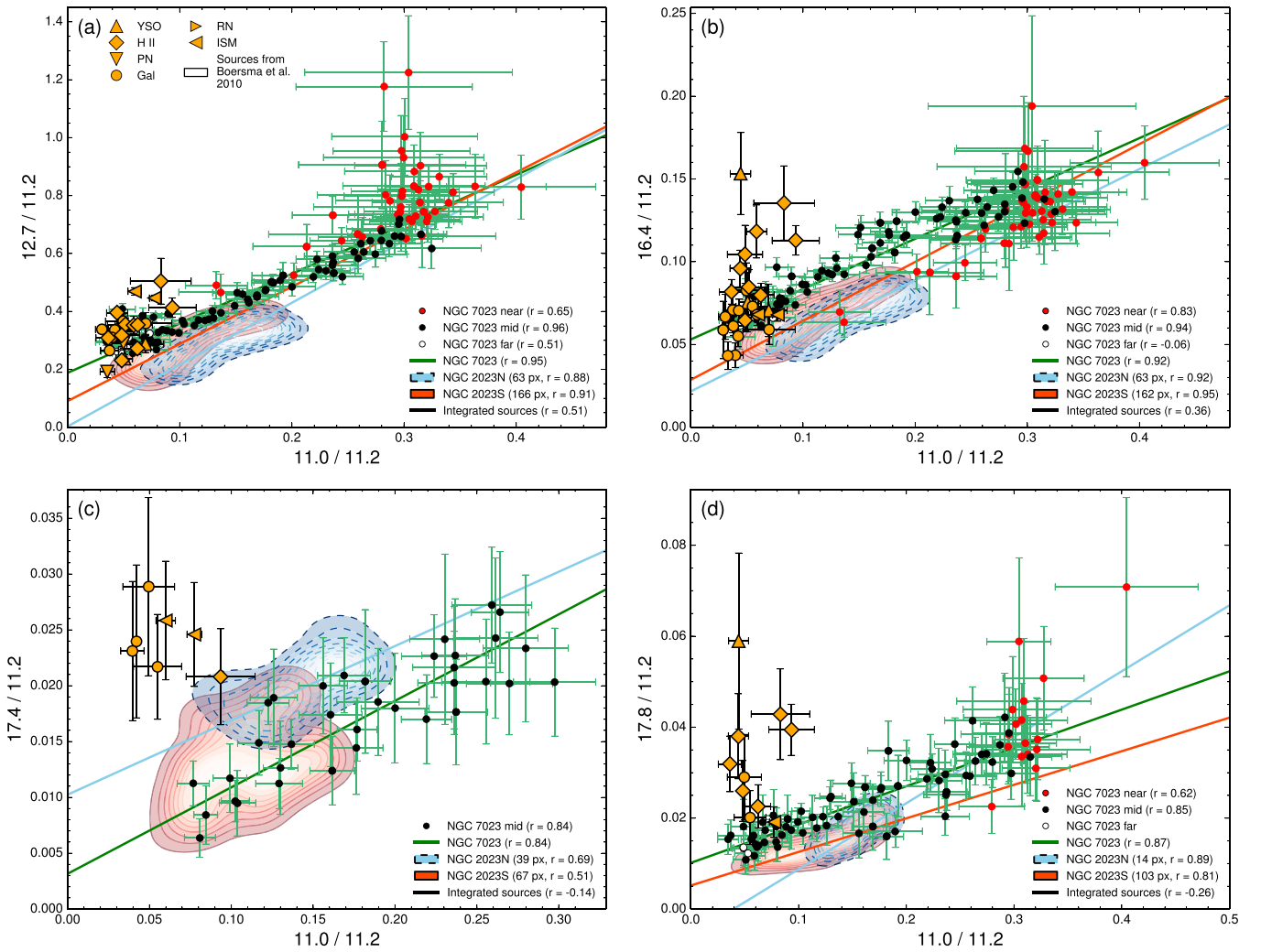


Figure 7. Correlation plots of the 12.7, 16.4, 17.4, and 17.8 μm bands vs. the 11.0 μm band.

the detection criteria. The 12.7 μm band was previously observed to correlate with the 16.4 μm band in NGC 2023 (Paper I; $r = 0.92$ in the southern map, $r = 0.88$ in the northern map) and in NGC 7023 (Boersma et al. 2014b; their Figure 9).

Correlation with the 6.2 μm band. We examine the flux ratios of the 16.4 and 6.2 μm bands in Figure 6 for the integrated sources in our sample. The 6.2 μm band cannot be measured in the SH RNe data as the wavelength coverage begins at $\sim 10 \mu\text{m}$. Data from Boersma et al. (2010) are included, where we have replaced the authors' average SINGS galaxy data point with our individual SINGS sources. We observe no linear correlation ($r = 0.11$), though we note the lower-right quadrant is devoid of sources. Furthermore, we identify the H II regions as occupying the upper-left quadrant of this figure. If these are excluded from the data set, a modest correlation is observed ($r = 0.47$). A mostly linear trend ($r^2 = 0.76$) between these bands has been identified in NGC 7023 by Boersma et al. (2014b), their Figure 10, albeit with some residual curvature. Our measurements are consistent with their measurements at low abscissa/ordinate values.

Since we detect a correlation between the 16.4 and 12.7 μm bands, and essentially none between the 16.4 and 6.2 μm bands, we should expect no correlation between the 6.2 and

12.7 μm bands for consistency. We indeed detect no such correlation in our data alone. However, the 6.2 and 12.7 μm PAH bands have been observed to correlate for a sample of integrated sources of various object types (Hony et al. 2001) and within the RNe NGC 7023 (Boersma et al. 2014b) and NGC 2023 (Paper II). The lack of such a correlation in our sample of integrated sources is likely due to the small range of ratios probed by our data, as they span a small range of ratios relative to Hony et al. (2001).

Correlations with the 11.0 μm band. We observe that the 16.4, 17.4, and 17.8 μm bands correlate with the 11.0 μm band in NGC 2023 and NGC 7023 (Figure 7). The NGC 7023 pixels furthest from and nearest to the star tend to individually cluster, while the region containing the peak of the PAH emission shows linear correlations between band intensity ratios (regions defined in Figure 10). This clustering has been previously observed, for example in Boersma et al. (2014b). The 12.7 μm band is also included for comparison, and the RNe display strong correlations between the 12.7 and 11.0 μm bands ($r \geq 0.90$). The integrated sources show no clear correlations between the 11.0 μm band and the 12.7, 16.4, 17.4, and 17.8 μm bands, as they tend to cluster near $11.0/11.2 \sim 0.060$. They tend to be consistent with the observed RNe correlations for the 12.7 and 16.4 versus

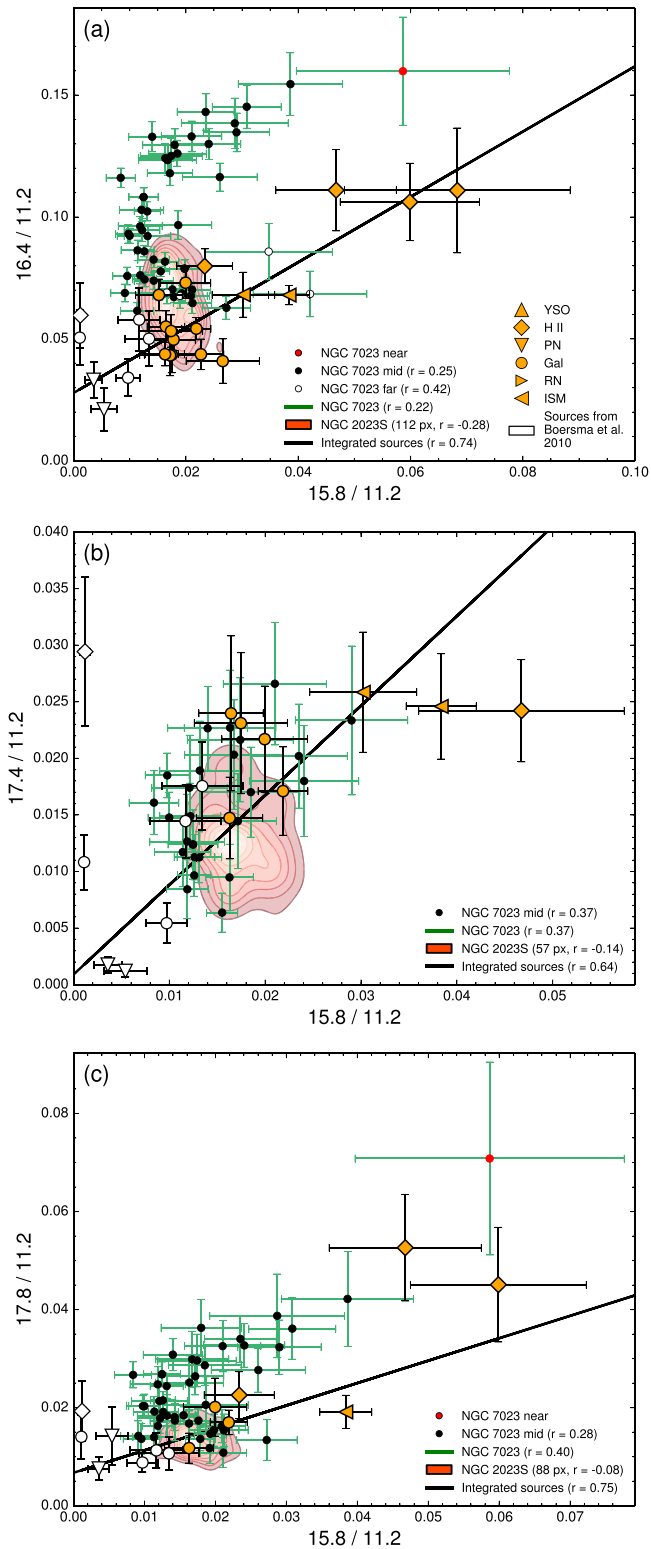


Figure 8. Correlation plots between the 11.2, 15.8 μm bands and the 15–20 μm plateau (panels (a), (b), (c), respectively).

11.0 μm bands, but they deviate for the 17.8 μm and especially the 17.4 μm band.

4.1.2. The 15.8 μm Band

The 16.4, 17.4 and 17.8 μm bands do not appear to correlate with the 15.8 μm band (Figure 8). NGC 2023S shows no

correlation between these bands (e.g., $r = -0.28$ when comparing the 15.8 and 16.4 μm bands) and NGC 2023N has too few detections to be represented here (Papers I and II). NGC 7023 generally appears to have a similar distribution to NGC 2023S, with no overall correlation (e.g., $r = 0.22$). However, NGC 7023 does seem to exhibit a “C”-shaped distribution in the 16.4 versus 15.8 μm band intensity correlation plot. This may be indicative of a relationship present at 16.4/11.2 ratios greater than 0.12, and 17.8/11.2 ratios greater than 0.03, but it is not conclusive. The integrated sources are shown to occupy three regions of the correlation plots: the data of Boersma et al. (2010) at low abscissa values; the SINGS galaxies at an intermediate position; and H II regions or cirrus sources toward the upper-right quadrant. Together these produce a correlation (with coefficient $r = 0.74$) but this is possibly spurious. Specifically, in the previous plots (Figure 4), the identified correlations can be seen both individually within our sample and individually in the sample of Boersma et al. (2010). In contrast, these correlations involving the 15.8 μm band are not present in either sample in isolation. Additionally, the closeness of the [Ne III] 15.56 μm line to the 15.8 μm PAH band in low-resolution spectra affects how well the PAH band can be measured. This is compounded because the 15.8 μm PAH band is weak and is near the inflection point of the rising 15–18 μm continuum; the error on the continuum is not taken into account in the 3σ cut-off. Finally, the Pearson correlation coefficient is known to be sensitive to outlying points (Devlin et al. 1975), which is why the measured coefficients here are not necessarily meaningful, unlike in Figure 4.

The 15.8 and 11.2 μm bands were shown to correlate in NGC 2023 (Paper I). We revisit this relationship in Figure 9(a). The data near the peak PAH emission region (i.e., in the middle of the NGC 7023 map, see Figure 10) are shown to correlate slightly ($r = 0.46$) and exhibit a gradient consistent with that in NGC 2023S. No correlation is identified for the integrated sources, though H II regions tend to lie at relatively high 15.8/12.7 ratios when compared to evolved stars or galaxies. The derived fluxes of the 15.8 and 12.7 μm bands are influenced by the presence of the [Ne II] 12.81 μm and [Ne III] 15.56 μm emission lines. These lines are present in H II regions and PNe and may influence or explain the observed discrepancy. Figures 9(b) and (c) compare the emission of the 15–18 μm plateau to those of the 11.2 and 15.8 μm bands, respectively, which were shown to correlate in NGC 2023 (Paper I). We find that NGC 7023 has similar correlations within its peak emission region; the other NGC 7023 regions do not show a clear correlation by themselves but they are consistent with the correlation seen in the NGC 7023 peak (“mid”) and NGC 2023. The integrated sources show no linear trend but there is significant clustering near the position (Plat./12.7, 11.2/12.7) \sim (1.5, 3.5).

4.2. Spatial Distribution of 15–20 μm PAH Emission

4.2.1. Map Morphology

We have thus far focused solely on correlations between bands. Paper II finds that the tightness of a correlation between any two bands is related to their spatial coincidence. However, even two bands with different spatial distributions could retain high correlation coefficients (e.g., the 8.6 and 7.7 μm bands,

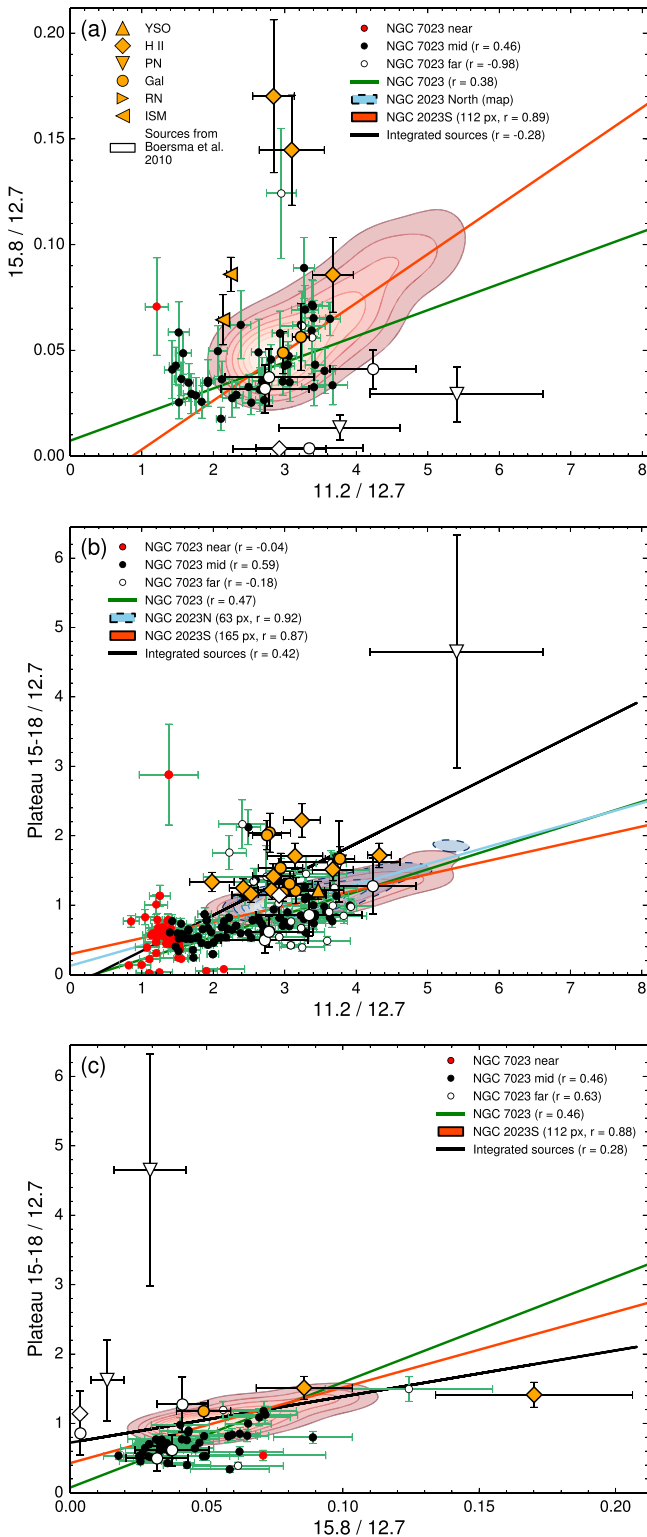


Figure 9. Correlation plots involving the 11.2 and 15.8 μm bands and the 15–18 μm plateau. (a) The 15.8 and 11.2 μm bands, normalized to the 12.7 μm PAH flux, correlate in RNe. (b), (c) 15–20 μm plateau correlations with the 11.2 and 15.8 μm bands in RNe.

with $r = 0.936$; Paper II). It is therefore important to determine if the correlations we identify are corroborated by their spatial morphologies. To do this, we examine the spectral map of NGC 7023 (Figure 10) and compare it with the spectral map of NGC 2023 (Papers I and II). The 16.4 μm data from this

spectral cube has been previously examined by Sellgren et al. (2007), and the 11.0, 11.2, 12.7, 16.4 μm bands and plateau emission by Boersma et al. (2013, 2014b, 2015). Additionally, zones parallel to the PDR front have been identified by Berné & Tielens (2012) and Boersma et al. (2014b); we introduce three such zones in Figure 10.

The spatial distributions of the 12.7, 16.4 and 17.8 μm bands are very similar in appearance. Each of these is seen to be displaced slightly toward the irradiating star relative to the 11.2 μm band. The 17.8 μm band is slightly more compact than the 12.7 and 16.4 μm bands; we note it also has a limited S/N in comparison. In NGC 2023, the 12.7 and 16.4 μm bands are also nearly identical in appearance, and the 17.8 μm band is mildly more compact. The 17.4 μm band has some apparent differences from the 12.7, 16.4 and 17.8 μm bands in the spatial maps, despite correlating with these bands: its emission is more compact and appears to peak 10'' closer to the exciting star in both NGC 7023 and NGC 2023, though the 17.4 μm band has a limited S/N in NGC 7023. The 11.0 μm band is also displaced closer to the exciting star to a similar degree in both RNe. The 17.4 μm band appears identical to the 11.0 μm band in NGC 2023 prior to removing the C_{60} component; after correction, the 17.4 μm band is slightly more compact than the 11.0 μm band.

The 11.2 μm band and the 15–18 μm plateau have coincident peak positions in both RNe, while the 15.8 μm band peaks slightly further distant from the star. The 15.8 μm band is much less extended than the 11.2 μm band and the plateau in NGC 7023, but it is only reliably measured in a small portion of the map due to its low S/N. In NGC 2023, the 15.8 μm band has a higher S/N and it shows a spatial distribution extremely close to that of the 11.2 μm band. The 15–18 μm plateau in NGC 2023 is much broader in extent.

4.2.2. PAH Emission Variability with Projected Distance

In order to investigate the change in PAH emission with projected distance from the illuminating star, we introduce radial slices or cuts across the maps of NGC 7023 and NGC 2023 (Figures 10 and 11) and analyze the individual band intensities as a function of the strength of the radiation field (Figures 12 and 13).

NGC 7023 is irradiated by HD 200775, a star of spectral type B2.5 Ve (Finkenzeller 1985), of effective temperature $17000 \text{ K} \pm 1000 \text{ K}$ (Baschek et al. 1982). We find the strength of the FUV radiation field, G_0 , to be 1.2×10^5 at 12'' and 1.4×10^4 at 35'' from HD 200775.⁵ This is consistent with Berné & Tielens (2012), who adopted values of $1 \pm 0.7 \times 10^5$ at 12'' and $1 \pm 0.7 \times 10^4$ at 35''.

The slices of NGC 7023 show that the 11.2 and 15.8 μm bands and the 15–18 μm plateau peak furthest from the star, at a projected distance, d , of 49'', or $G_0 \sim 7.0 \times 10^3$. The 12.7, 16.4 and 17.8 μm bands peak closer to the star, at $d \sim 39''$ –44'', or $G_0 \sim 11 \times 10^4$ – 8.5×10^3 . The 17.4 μm band peaks at $d \sim 40''$ ($G_0 \sim 1.2 \times 10^4$) and the 11.0 μm band has a wide peak from $d \sim 30''$ –39'', corresponding to $G_0 \sim 1.9 \times 10^4$ – 1.1×10^4 . The 17.4 μm band profile is much narrower than the

⁵ G_0 is the FUV flux between 6 and 13.6 eV, expressed in terms of the Habing field, $1.2 \times 10^{-4} \text{ erg s}^{-1} \text{ cm}^{-2} \text{ sr}^{-1}$ (Habing 1968). We use the formulation of Tielens (2005): $G_0 = 625 \frac{L_\chi}{4\pi d^2}$, where L is the luminosity of the star, χ is the luminosity fraction between 6–13.6 eV, and d is the distance from the star. χ was determined by evaluating a blackbody of effective temperature corresponding to the appropriate stellar spectral type.

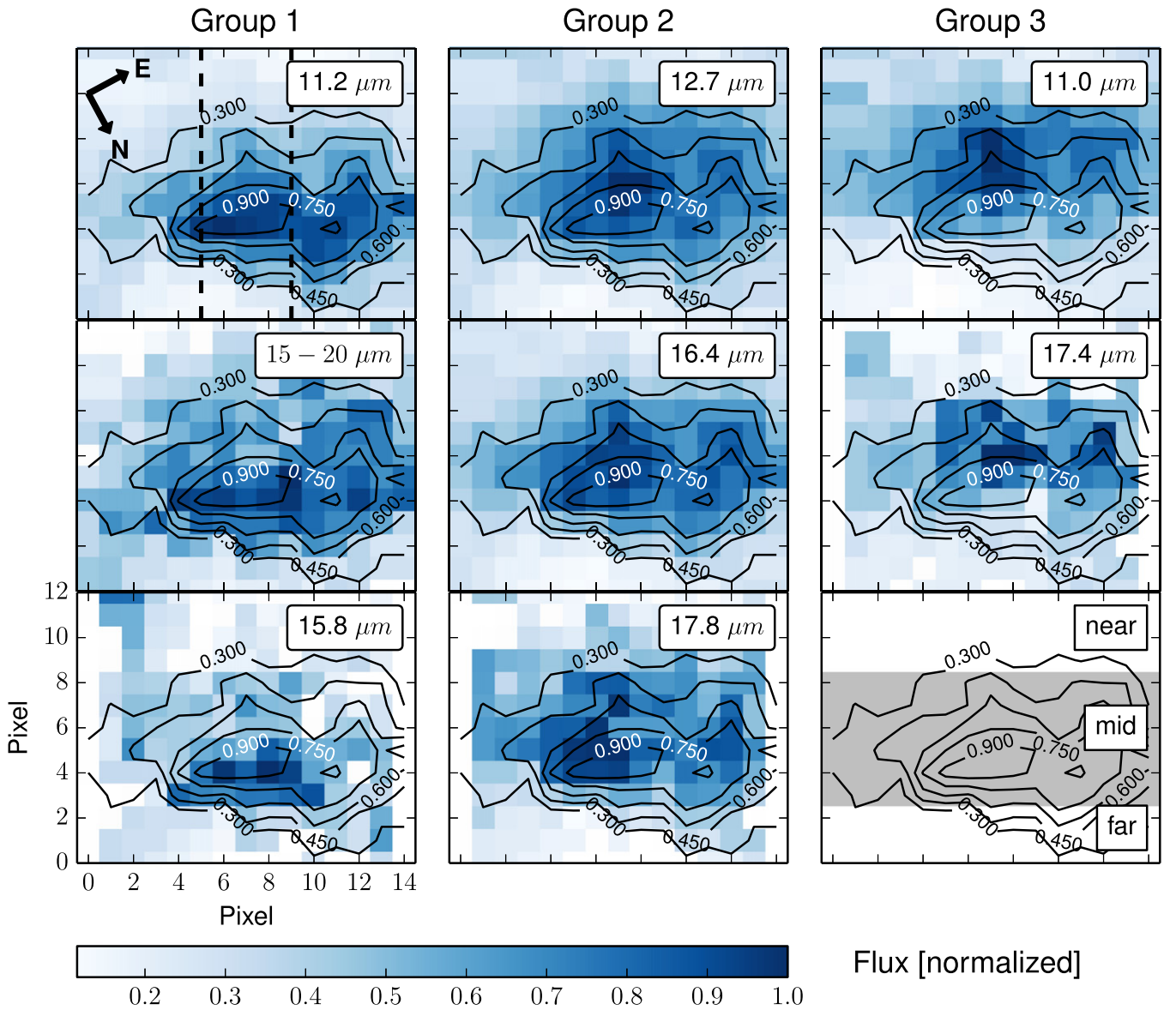


Figure 10. Maps of the normalized PAH band fluxes toward NGC 7023 (13×15 pixels). Maps have been rotated 20° such that the star is at the top of each panel in this orientation. The original field of view is as indicated in Figure 1. The black contours are constructed from the $11.2 \mu\text{m}$ band flux, normalized to unity. Bands are organized into vertical groupings (columns) based on similar characteristics (see the text). The vertical dashed lines (shown only on the $11.2 \mu\text{m}$ map) denote the region used for the five pixels-wide radial cut (Figure 12). We introduce in the lower-right panel three simple zones to distinguish regions of NGC 7023 data present in the correlation plots.

$11.0 \mu\text{m}$ emission, but it is aligned with the far edge of the $11.0 \mu\text{m}$ band. Slices of the 16.4 and $18.9 \mu\text{m}$ bands in NGC 7023 were presented by Sellgren et al. (2007). These authors observed the $16.4 \mu\text{m}$ emission to peak at approximately $36''$ distant from the star. We observe this peak to lie more distant, near $44''$, but we use a different decomposition method. Overall, the spatial profiles of the 12.7 , 16.4 , and $17.8 \mu\text{m}$ bands are broader and more symmetric than those of the other bands. We find that we can reproduce the profiles of the 12.7 and $16.4 \mu\text{m}$ bands extremely well by adding the 11.0 and $11.2 \mu\text{m}$ profiles and renormalizing the result (see Figure 12).

We perform a similar analysis on NGC 2023S, whose data have higher S/N and overall intensities than NGC 2023N's (Figure 13). NGC 2023 is illuminated by a B1.5 V star (Mookerjee et al. 2009). We derive G_0 values in a similar manner as for NGC 7023. The PAH transitions occur from $G_0 \sim 1.5 \times 10^3$ – 3.0×10^3 , in rough agreement with the estimates

of 10^3 – 10^4 in the literature, albeit on the low end (Sheffer et al. 2011, Paper I). The spatial stratification seen in NGC 7023 is also present in NGC 2023S. However, the transition occurs at quite different values of G_0 than NGC 7023. This suggests that our simple approximation of G_0 is not accurate enough and other parameters such as density, gas temperature and/or projection effects may play a role. Specifically, the 11.0 and $17.4 \mu\text{m}$ bands peak nearest the star, with the $11.0 \mu\text{m}$ band showing a broad peak from approximately $80''$ – $95''$ distant ($G_0 \sim 2.9 \times 10^3$ – 2.1×10^3), and the $17.4 \mu\text{m}$ band being more compact near a distance of $84''$ ($G_0 \sim 2.6 \times 10^3$). The 11.2 , $15.8 \mu\text{m}$ bands and the 15 – $18 \mu\text{m}$ plateau all peak near $d \sim 111''$ ($G_0 \sim 1.5 \times 10^3$), but we note the plateau is slightly broader. The 12.7 and $16.4 \mu\text{m}$ bands are flat from $d \sim 80''$ – $105''$ ($G_0 \sim 2.9 \times 10^3$ – 1.7×10^3), again broader than the other emission bands, as in NGC 7023. The $17.8 \mu\text{m}$ band is similar to the 12.7 and $16.4 \mu\text{m}$ bands but it peaks closer to the

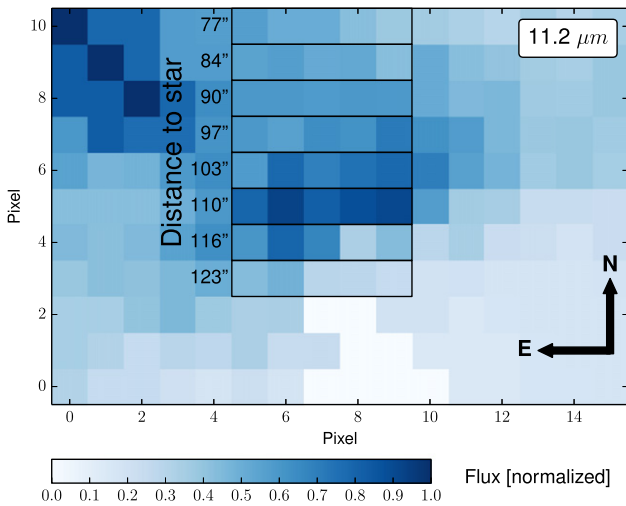


Figure 11. Normalized $11.2 \mu\text{m}$ PAH intensity map of NGC 2023S (Papers I and II). These data have been rotated 35° counter-clockwise to be roughly perpendicular to the irradiating star’s radial vector. The outlined regions identify the five-pixel-wide apertures used to create the radial slices. The exciting star is located upward in this projection, with estimated distance to each aperture as shown.

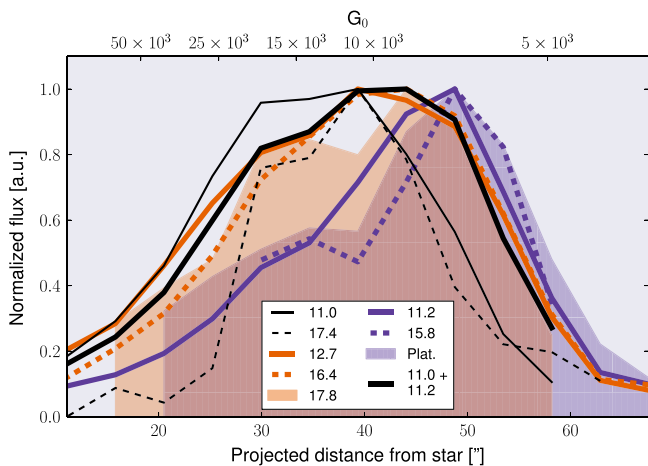


Figure 12. Normalized PAH intensity along a projected cut across NGC 7023 directed toward the irradiating source, extracted at 12 positions, using a five-pixel-wide extraction aperture (see Figure 10). The colors indicate groupings of bands with similar peak positions and/or spatial profiles along the cut.

star ($80''$ – $95''$, $G_0 \sim 2.9 \times 10^3$ – 2.0×10^3), with a profile near that of the $11.0 \mu\text{m}$ band. Again, the 12.7 and $16.4 \mu\text{m}$ band profiles are well realized by summing and renormalizing the 11.0 and $11.2 \mu\text{m}$ bands, albeit with a slight overestimate near $110''$.

5. DISCUSSION

5.1. Interpretation

We first summarize the observational results, and subsequently, we discuss the implications in terms of charge and molecular structure, based on comparison with theoretical studies. The observational results consist of PAH band intensity correlations for integrated and extended sources, as well as spatial measurements of PAH emission in spectral maps of NGC 7023 and NGC 2023.

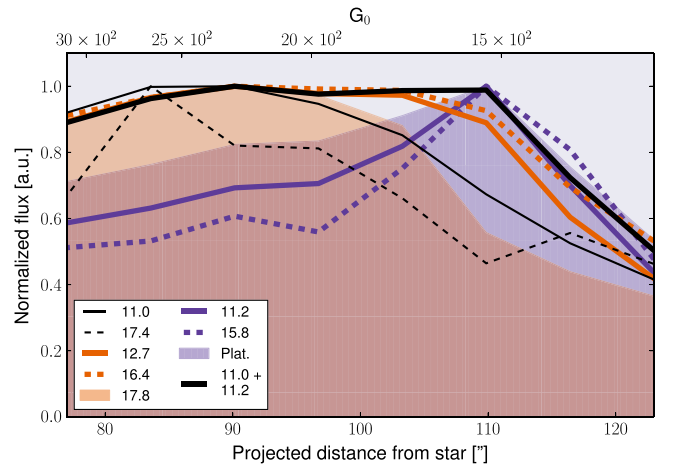


Figure 13. Normalized PAH intensity along a projected cut across NGC 2023S directed toward the irradiating source, extracted at 8 positions, using a five-pixel-wide extraction aperture (see Figure 11). The colors indicate groupings of bands with similar peak positions and/or spatial profiles along the cut.

Correlations. The 16.4 , 17.4 , and $17.8 \mu\text{m}$ band fluxes are inter-correlated in all environments. Furthermore, each of these three bands correlates with the $12.7 \mu\text{m}$ band in the RNe. Among the sample of integrated sources, the 16.4 and $17.8 \mu\text{m}$ bands correlate with the $12.7 \mu\text{m}$ band only in H II regions. Together, these four bands (12.7 , 16.4 , 17.4 , and $17.8 \mu\text{m}$) correlate strongly with the $11.0 \mu\text{m}$ band in RNe. The $15.8 \mu\text{m}$ band does not correlate with any of these bands, leaving it as the odd one out. However, the $15.8 \mu\text{m}$ band is inter-correlated in RNe with the 15 – $18 \mu\text{m}$ plateau and the $11.2 \mu\text{m}$ band. Finally, the 16.4 and $6.2 \mu\text{m}$ bands show no overall linear correlation for the integrated sources, though if we exclude H II regions from this analysis they show a modest correlation, in line with results found in the literature (Boersma et al. 2010, 2014b). Our data are also isolated to relatively low ordinate and abscissa values, falling upon the lower end of the relationship found by Boersma et al. (2014b).

Spatial maps. The RNe spatial maps show a common morphology between the 12.7 , 16.4 , and $17.8 \mu\text{m}$ bands. Similarity is also observed between the 11.2 and $15.8 \mu\text{m}$ bands and the 15 – $18 \mu\text{m}$ plateau. Lastly, the 11.0 and $17.4 \mu\text{m}$ bands appear to peak in similar locations. We invoked radial cuts to isolate the spatial origin of each band to examine these similarities. The 11.0 and $17.4 \mu\text{m}$ bands peak closest to the star, in similar locations, though the $11.0 \mu\text{m}$ band’s spatial profile is wider. The 11.2 , $15.8 \mu\text{m}$ bands and 15 – $18 \mu\text{m}$ plateau peak furthest from the star, sharing very similar profiles. The 12.7 and $16.4 \mu\text{m}$ band profiles peak in an intermediate location, with very similar shapes. The $17.8 \mu\text{m}$ band follows the 12.7 and $16.4 \mu\text{m}$ bands in NGC 7023 but its profile is more similar to that of the $11.0 \mu\text{m}$ band in NGC 2023S. We observe that the profiles of the 12.7 and $16.4 \mu\text{m}$ bands (and the $17.8 \mu\text{m}$ band in NGC 7023) can be reproduced by averaging the spatial profiles of the 11.0 and $11.2 \mu\text{m}$ bands.

5.1.1. Charge

We first examine the observational results in the context of ionization states. The 11.0 and $11.2 \mu\text{m}$ PAH bands have been firmly assigned to cationic and neutral PAHs, respectively (Hudgins & Allamandola 1999; Hony et al. 2001). The

similarities of the $15.8\ \mu\text{m}$ band to the $11.2\ \mu\text{m}$ band in the maps, cuts, and the fact that they correlate suggest that the $15.8\ \mu\text{m}$ band originates in neutral PAHs. Likewise, the observational data suggests the $17.4\ \mu\text{m}$ band is coincident with the $11.0\ \mu\text{m}$ emission, with which it correlates; we therefore associate the $17.4\ \mu\text{m}$ band with cationic PAHs. The 12.7 , 16.4 , and $17.8\ \mu\text{m}$ bands are self-similar in the maps and cuts, and have an extent that envelops both the 11.0 and $11.2\ \mu\text{m}$ bands. In conjunction with the correlation plots, these data suggest that the 12.7 , 16.4 , and $17.8\ \mu\text{m}$ bands arise from both cationic and neutral PAHs.

Paper I suggested that the $17.8\ \mu\text{m}$ band arises from both neutral and ionized PAHs, which we here confirm. Furthermore, Paper I concluded that the $16.4\ \mu\text{m}$ band is from species cospatial with the cationic portion of the emitting PAH population. This result was strongly supported by the results of Boersma et al. (2014b); the authors however noted that residual curvature in their correlations plots indicated that other population changes are at play. Here we identify two components of the $16.4\ \mu\text{m}$ band: one cospatial with cationic PAHs and one cospatial with neutral PAHs. The $12.7\ \mu\text{m}$ band was also shown to be coincident with PAH cations in Paper I. Rosenberg et al. (2011) used blind signal separation to identify two components of the $12.7\ \mu\text{m}$ band, which they associate with neutrals and cations. Boersma et al. (2014b) supported their assignment; this work also supports a combined neutral and cationic origin for the $12.7\ \mu\text{m}$ band. Paper I suggested the $17.4\ \mu\text{m}$ bands arises from doubly ionized PAHs and/or a subset of the cationic PAH population. We attribute the $17.4\ \mu\text{m}$ bands to cations generally, and not necessarily a particular subset. The discrepancy may be due to how each paper traces cations: we use the $11.0\ \mu\text{m}$ band as a tracer of cations here, whereas Paper I used the 6.2 and $7.7\ \mu\text{m}$ bands as tracers. Paper II finds that there are two populations contributing to the $7.7\ \mu\text{m}$ band (and thus the $6.2\ \mu\text{m}$ band, due to its similar morphology), and so the $7.7\ \mu\text{m}$ band may not be an ideal tracer of PAH cations. Additionally, Boersma et al. (2015) show that the $7.7\ \mu\text{m}$ PAH band strength may not be a reliable tracer for PAH cations. We attribute the $15.8\ \mu\text{m}$ band to neutral PAHs, in agreement with Paper I.

Theoretical studies of PAH vibrational modes have given us clues about the origins of the $15\text{--}20\ \mu\text{m}$ emission bands (Boersma et al. 2010; Ricca et al. 2010). These often make use of the NASA Ames PAH IR Spectroscopic Database⁶ (Bauschlicher et al. 2010; Boersma et al. 2014a). Specifically, the $16.4\ \mu\text{m}$ band appears to arise from a mixture of out-of-plane and in-plane vibrations, particularly due to elongation and compression modes (Ricca et al. 2010). The $17.4\ \mu\text{m}$ band originates in a mixture of C–C–C in-plane and out-of-plane modes and the $17.8\ \mu\text{m}$ band is attributed to a mixture of C–H and C–C–C out-of-plane bending. The origin of the $15.8\ \mu\text{m}$ band is unclear, though emission at $15.4\ \mu\text{m}$ by C–C–C in-plane bending modes was identified by Ricca et al. (2010); this may or may not correspond to the astronomical $15.8\ \mu\text{m}$ band. Using these analyses, we assert that the intrinsic intensities of the 15.8 , 16.4 , 17.4 or $17.8\ \mu\text{m}$ bands do not vary by more than approximately a factor of 2 between charge states (anions, neutrals, cations). This estimate is based on Figure 13 of Ricca et al. (2010), which presents average spectra for all PAHs in the Ames database containing more than 50 carbon atoms, separated by ionization

state, and Figure 15 of Boersma et al. (2010), showing the intrinsic intensities for different charge states of $\text{C}_{96}\text{H}_{24}$. In general then, the $15\text{--}20\ \mu\text{m}$ emission bands produce intensity variations that are much more subdued than the variations observed in the $3\text{--}12\ \mu\text{m}$ range, which span approximately one order of magnitude (Allamandola et al. 1999). Emission by anions, neutrals and cations is expected for all four $15\text{--}20\ \mu\text{m}$ bands in the database (Ricca et al. 2010). The $16.4\ \mu\text{m}$ band is expected to be twice as strong for cations than for the other charge states (Bauschlicher et al. 2010; Ricca et al. 2010). The $17.8\ \mu\text{m}$ band appears to have similar intensities in each charge state, while the $17.4\ \mu\text{m}$ band should be strongest in anions by a factor of two (Ricca et al. 2010). These authors computed spectra for eight neutral PAHs and noted similar intensities between the 17.4 and $17.8\ \mu\text{m}$ band, possibly implying a correlation; such a correlation is observed in this work. Lastly, emission was observed at $15.4\ \mu\text{m}$ by (Ricca et al. 2010), with cations exceeding the intensities of neutrals and anions by a factor of two, but it is unknown if this emission corresponds to the astronomical band at $15.8\ \mu\text{m}$.

Setting aside anions due to their expected very low abundances, we note that the prediction of similar emission intensities of the $17.8\ \mu\text{m}$ band between cations and neutral PAHs is consistent with our observational results. This can be seen in the spatial maps and cuts, in which the $17.8\ \mu\text{m}$ band’s spatial profile encompasses the 11.0 and $11.2\ \mu\text{m}$ bands, centered between them. The $16.4\ \mu\text{m}$ band, which is predicted to be twice as strong in cations than neutrals, is however somewhat at odds with the observational data: we observe it has the same spatial profile as the $17.8\ \mu\text{m}$ band, with no preference or tendency toward the $11.0\ \mu\text{m}$ emission over the $11.2\ \mu\text{m}$ emission. This suggests it should arise from a similarly balanced mixture of cations and neutrals from which the $17.8\ \mu\text{m}$ band originates. The $17.4\ \mu\text{m}$ band is predicted by the database to have similar emission intensities between cations and neutral PAHs, which is inconsistent with our assignment solely to cations. Lastly, the database $15.4\ \mu\text{m}$ band is seen to be cation-dominant, at odds with the neutral character of the $15.8\ \mu\text{m}$ astronomical band from the observational data. It may simply be the case that these two bands do not correspond to the same emission feature. Other possibilities for the observed inconsistencies may include variable PAH population abundances, incompleteness and/or poor representation of these particular (sub-)populations in the database, or simply that our data are not sufficiently sensitive to probe variations at the scale of two-to-one. An examination of the radial cuts shows the latter point to be true.

5.1.2. Molecular Structure

Molecular structure determines which vibrational modes are available to any particular PAH, but it is not known a priori how much of an influence structure will play in driving band intensity correlations on the whole. Some headway has been made in this area, in so far as particular band attributions have been suggested. The $16.4\ \mu\text{m}$ band has been attributed to PAHs containing pendent rings or “pointed” edges (e.g., Van Kerckhoven et al. 2000; Peeters et al. 2004; Boersma et al. 2010; Ricca et al. 2010). The former are single cycles that attach to the carbon skeleton through two shared carbon atoms, while the latter are corners that naturally arise in parallelogram-shaped PAHs, attached through three shared carbon atoms. The $16.4\ \mu\text{m}$ band correlates well with the

⁶ <http://www.astrochem.org/pahdb/>

17.8 μm band, which appears to be somewhat structure insensitive: the 17.8 μm band was present in all eight large neutral PAHs studied by Ricca et al. (2010), despite encompassing a variety of structures, including some with pointed edges. The 12.7 μm band, which correlates well with both the 16.4 and 17.8 μm emission, is associated with a combination of duo and trio C–H out-of-plane modes (Hony et al. 2001; Bauschlicher et al. 2009, 2010). Recently, this band was suggested to specifically originate in PAHs having an armchair-like structure (Candian et al. 2014). As pendent rings and pointed edges naturally constitute duos and trios, it is then possible that the 12.7 and 16.4 μm bands naturally correlate due to these common features. The 17.8 μm band is not known to have a dependence on duos or trios, but it has been suggested that it is a molecule-independent feature (Ricca et al. 2010), which may explain why it correlates with the 12.7 and 16.4 μm bands.

The 17.4 μm band, which correlates with the 12.7, 16.4 and 17.8 μm bands, generally appears to show the strongest emission intensities in compact PAHs (Bauschlicher et al. 2010; Ricca et al. 2010). The 15.6 μm band (which may or may not correspond to the astronomical 15.8 μm band) has been suggested to arise from vibrations of pendent rings (Boersma et al. 2010). Pendent rings are also suggested as one possible origin for the 16.4 μm band. If both the 15.8 and 16.4 μm bands are (at least in part) due to pendent rings, one would expect an intensity correlation, depending on environmental conditions (which we cannot speculate on here). In general the observational data show no such correlation between these bands, though there is a slight hint of a linear correlation when the ratio of 16.4/11.2 exceeds 0.12 (see Figure 8). The correlation of the 15.8 μm band with the 11.2 μm band is suggestive of large molecules, but it is known that the emission intensity of the 15.8 μm band decreases with increasing PAH size in the NASA Ames PAH IR Spectroscopic Database (Bauschlicher et al. 2010; Ricca et al. 2010; Boersma et al. 2014a). Finally, Boersma et al. (2010) examined classes of PAHs, including compact, irregular, and pentagon-containing PAHs. Minor systematic trends were observed, including the fact that irregular PAHs tend to have richer and more variable spectral features when compared to compact PAHs. As molecule size increased, compact PAHs exhibited little variation in the types of C–C–C vibrational modes that were active, whereas the complex edge structure of irregular PAHs facilitated a larger variety of C–C–C vibrational modes (Boersma et al. 2010). Even with this knowledge, at the present there is no clear mapping between molecular structure and the observational data.

5.1.3. Summary

The exact balance between charge and molecular structure in driving the observed correlations of the 15–20 μm bands cannot be discerned. However, the maps and radial cuts appear to cleanly separate these bands into those dominated by cations (11.0, 17.4 μm), neutrals (11.2, 15.8 μm , 15–18 μm plateau), or a combination of the two (e.g., 12.7, 16.4, 17.8 μm bands). This suggests charge is the dominant factor driving these correlations, though there are indications that some bands should correlate due to structural arguments (e.g., the 12.7 and 16.4 μm bands). Ultimately, theory points toward a mixture of highly variable emission features (e.g., Boersma et al. 2010, their Figures 11–15), whereas in space we observe a relatively simple picture of four bands and one underlying plateau. This simplicity may reflect a basic commonality of the carriers, or

suggest that a relatively small collection of stable molecules are responsible for the observed emission bands (Boersma et al. 2010). The latter is known as the *grandPAH* hypothesis (Andrews et al. 2015).

5.2. Statistics of the 15–20 μm Emission

First we determine if the relative emission strengths of the 5–15 μm bands in our sample are consistent with similar measurements in the literature (Peeters et al. 2002). We accomplish this by measuring the fractional contribution of the 6.2, 7.7, 8.6 and 11.2 μm bands to the total MIR emission (which we define here as the total flux emitted by these bands) for nine H II regions and fifteen galaxies in our sample. Since Peeters et al. (2002) only had two galaxies in their sample, we use the H II regions as a direct point of comparison. Our results are presented in Figure 14, panel (a). We find that the H II regions are consistent with those of Peeters et al. (2002), whose data is presented in panel (b), and there is no discrepancy between H II regions and galaxies in our sample. Note that Peeters et al. (2002) included the 3.3 μm band and not the 8.6 μm band in their analysis, whereas we do the opposite (as our spectra start at 5 μm). The 3.3 and 8.6 μm bands are quite weak (less than 10% of the total MIR emission in both studies) and should therefore not strongly influence the analysis.

The same analysis is performed for the “FIR” features, i.e., the 15.8, 16.4, 17.4, and 17.8 μm bands and the 15–18 μm plateau, shown in Figure 14, panel (c). Due to the inconsistent detections of the 15.8, 17.4, and 17.8 μm bands, the 16.4 μm band and the 15–18 μm plateau are used together as a proxy for the total FIR PAH flux. The 15.8, 16.4, and 17.8 μm bands have fractional strengths in H II regions of $7 \pm 4\%$, $16 \pm 2\%$, and $6 \pm 1\%$, respectively. In galaxies, these are systematically lower, with values $4 \pm 1\%$, $11 \pm 3\%$, and $3 \pm 1\%$, respectively. The 17.4 μm band is observed to have similar strengths between H II regions and galaxies ($3 \pm 1\%$ in each). The plateau makes up the remainder of the measured fractional strengths. The observed inconsistency by object type may be due to underestimating the 17.4 μm PAH emission in H II regions or overestimating the 17.4 μm emission in galaxies. Neither would be surprising, as C₆₀ emission at 17.4 μm is common, and it can only be removed by measuring the 18.9 μm C₆₀ emission, which itself is blended with the [S III] 18.71 μm line. Recall the typical 17.4/18.9 μm C₆₀ band strength ratio is approximately 0.5 (Cami et al. 2010; Sellgren et al. 2010; Bernard-Salas et al. 2012). Another possibility is that the 15.8, 16.4 and 17.8 μm bands are all overestimated in H II regions, which requires a trio of systematic errors that we deem unlikely, as the same method was applied to both H II regions and galaxies. The third possibility is that these bands truly are systematically higher in H II regions than galaxies.

As a separate analysis, we investigate whether the MIR/FIR ratio depends on object type, where the 11.2 and 16.4 μm bands are used as proxies for the MIR and FIR emission, respectively. We therefore examined 490 low-resolution spectra of the SAGE-Spec sample and used the following selection criteria: (1) PAHs must be clearly present; (2) the spectra displayed no discontinuous jumps; (3) sources were less extended than $9''$ (which corresponds to the approximate size of the SL aperture at 6.2 μm); and (4) the 11.2 and 16.4 μm PAH bands must have 3σ detections. We identify 10 H II regions and 22 evolved stars as meeting these criteria. The H II regions have

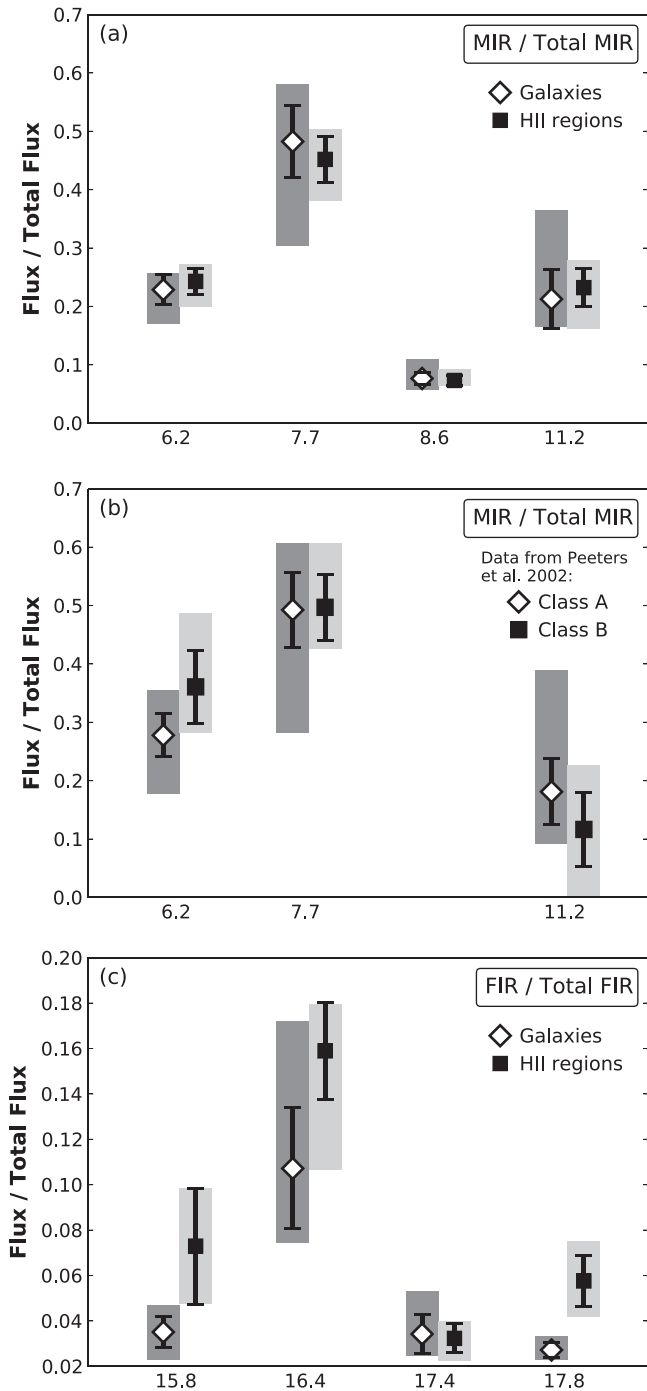


Figure 14. Statistical summary of the 5–15 μm and 15–20 μm PAH bands. The fraction of total flux in each band is illustrated by its mean (white diamond for galaxies, black square for H II regions), standard deviation (black line), and minimum and maximum values (denoted by the gray rectangles). (a) The 6.2, 7.7, 8.6, and 11.2 μm emission (called “MIR” here) are normalized to their combined total emission. (b) The same analysis, for class A and B sources, as presented in Peeters et al. (2002). Note that the authors included 3.3 μm emission, but did not have 8.6 μm emission. (c) The fractional emission in the “FIR” bands (15.8, 16.4, 17.4, 17.8 μm bands) are compared. The total FIR emission is considered to be the sum of the 16.4 μm and plateau emission. The plateau fraction ($\gtrsim 0.7$) is omitted for clarity.

a mean 16.4/11.2 ratio of 0.09 ± 0.02 . Evolved stars exhibited a ratio of 0.12 ± 0.05 , consistent with the H II regions. As such, we find no dependence on object type for the relative MIR and FIR band intensities in this analysis.

6. SUMMARY AND CONCLUSIONS

The 15–20 μm PAH emission bands have been investigated in 57 sources, comprised of LMC point sources from the SAGE-Spectroscopy survey, nearby galaxies from SINGS, two extended cirrus sources and a spectral map of NGC 7023. We also included the sample of Boersma et al. (2010) and spectral maps of NGC 2023 (Papers I and II). We investigated correlation plots of band flux ratios and examined the map morphologies of the RNe NGC 7023 and NGC 2023. We performed radial cuts across these maps to evaluate the spatial profiles of the 15–20 μm PAH emission. Our primary conclusions are as follows:

1. Correlation plots:

- (i) The 16.4, 17.4, and 17.8 μm bands are inter-correlated in all environments.
- (ii) Within the RNe we see that the 16.4, 17.4, and 17.8 μm bands further correlate with the 11.0 and 12.7 μm bands. In H II regions, the 12.7 μm band also correlates with the 16.4 and 17.8 μm bands.
- (iii) The 11.2 and 15.8 μm bands and the 15–18 μm plateau are inter-correlated in NGC 7023, consistent with results for NGC 2023 (Paper I). The 15.8 μm band does not correlate with the 11.0, 12.7, 16.4, 17.4, or 17.8 μm bands in general. Within a sub-region of NGC 7023 the 15.8 μm band appears to show a modest correlation with the 16.4, and 17.8 μm bands.

2. Spectral maps:

- (i) The maps show similar morphologies between the 11.0 and 17.4 μm bands, the 12.7, 16.4, and 17.8 μm bands, and the 11.2 and 15.8 μm bands with the 15–18 μm plateau.
- (ii) The radial slices in the RNe maps show that the spatial profiles of the 12.7, 16.4, and 17.8 μm bands can be reconstructed by averaging the 11.0 and the 11.2 μm band profiles.

3. Charge dominates: we attribute the 12.7, 16.4, and 17.8 μm bands to a combination of neutral and cationic molecules. The 17.4 μm band we attribute to cations, based on similarity of its spatial distribution to the 11.0 μm emission in the maps and radial cuts. Our results support the association of the 15.8 μm band with PAHs, specifically neutral PAHs (Paper I).

4. The 16.4/11.2 ratio in the general SAGE-Spec sample shows no dependence on object type. The fractional emission of the 15.8, 16.4, and 17.8 μm bands in H II regions are systematically higher than those in galaxies. The 17.4 μm band is the exception, which has similar fractional strengths in both environments.

With the significant number of sources in our sample, we were able to discover correlations between the 15–20 μm features that were not discernible in the much smaller sample studied by Boersma et al. (2010). The forthcoming *JWST* instrument MIRI will be an essential tool in furthering this analysis. Its large collecting area and increased spatial sensitivity will permit the construction of larger sample sizes, permitting further statistical analysis. Additionally, its improved spectral sensitivity will also allow us to examine the PAH band profiles in detail, with less line-blending than is possible with current data sets. These key improvements, in conjunction with theoretical and laboratory analysis,

may help disentangle the inter-related behaviors of the 15–20 μm bands.

We thank the anonymous referee for useful feedback. The authors thank J. D. Smith for supplying the SINGS data, as well as C. Boersma for supplying the data of their study. The authors also thank P. M. Woods for providing object classifications. The authors acknowledge support from NSERC discovery grant, NSERC acceleration grant and ERA. The IRS was a collaborative venture between Cornell University and Ball Aerospace Corporation funded by NASA through the Jet Propulsion Laboratory and Ames Research Center (Houck et al. 2004). This research has made use of NASA's Astrophysics Data System Bibliographic Services, and the SIMBAD database, operated at CDS, Strasbourg, France.

REFERENCES

- Allamandola, L. J., Hudgins, D. M., & Sandford, S. A. 1999, *ApJL*, **511**, L115
 Allamandola, L. J., Tielens, A. G. G. M., & Barker, J. R. 1989, *ApJS*, **71**, 733
 Andrews, H., Boersma, C., Werner, M. W., et al. 2015, *ApJ*, **807**, 99
 Baschek, B., Beltrametti, M., Koppen, J., & Traving, G. 1982, *A&A*, **105**, 300
 Bauschlicher, C. W., Jr., Boersma, C., Ricca, A., et al. 2010, *ApJS*, **189**, 341
 Bauschlicher, C. W., Jr., Peeters, E., & Allamandola, L. J. 2009, *ApJ*, **697**, 311
 Beasley, A. J., Ellingsen, S. P., Claussen, M. J., & Wilcots, E. 1996, *ApJ*, **459**, 600
 Bernard-Salas, J., Cami, J., Peeters, E., et al. 2012, *ApJ*, **757**, 41
 Bernard-Salas, J., Peeters, E., Sloan, G. C., et al. 2009, *ApJ*, **699**, 1541
 Berné, O., & Tielens, A. G. G. M. 2012, *PNAS*, **109**, 401
 Boersma, C., Bauschlicher, C. W., Allamandola, L. J., et al. 2010, *A&A*, **511**, A32
 Boersma, C., Bauschlicher, C. W., Jr., Ricca, A., et al. 2011, *ApJ*, **729**, 64
 Boersma, C., Bauschlicher, C. W., Jr., Ricca, A., et al. 2014a, *ApJS*, **211**, 8
 Boersma, C., Bauschlicher, C. W., Jr., Ricca, A., et al. 2015, *ApJ*, **806**, 121
 Boersma, C., Bregman, J., & Allamandola, L. J. 2014b, *ApJ*, **795**, 110
 Boersma, C., Bregman, J. D., & Allamandola, L. J. 2013, *ApJ*, **769**, 117
 Boulanger, F., Boissel, P., Cesarsky, D., & Ryter, C. 1998, *A&A*, **339**, 194
 Cami, J., Bernard-Salas, J., Peeters, E., & Malek, S. E. 2010, *Sci*, **329**, 1180
 Candian, A., Sarre, P. J., & Tielens, A. G. G. M. 2014, *ApJL*, **791**, L10
 Devlin, S. J., Gnanadesikan, R., & Kettenring, J. R. 1975, *Biometrika*, **62**, 531
 Finkenzeller, U. 1985, *A&A*, **151**, 340
 Galliano, F., Madden, S. C., Tielens, A. G. G. M., Peeters, E., & Jones, A. P. 2008, *ApJ*, **679**, 310
 Habing, H. J. 1968, *BAN*, **19**, 421
 Hony, S., Van Kerckhoven, C., Peeters, E., et al. 2001, *A&A*, **370**, 1030
 Houck, J. R., Roellig, T. L., van Cleve, J., et al. 2004, *ApJS*, **154**, 18
 Hudgins, D. M., & Allamandola, L. J. 1999, *ApJL*, **516**, L41
 Kemper, F., Woods, P. M., Antoniou, V., et al. 2010, *PASP*, **122**, 683
 Kennicutt, R. C., Jr., Armus, L., Bendo, G., et al. 2003, *PASP*, **115**, 928
 Mookerjee, B., Sandell, G., Jarrett, T. H., & McMullin, J. P. 2009, *A&A*, **507**, 1485
 Moutou, C., Verstraete, L., Léger, A., Sellgren, K., & Schmidt, W. 2000, *A&A*, **354**, L17
 Peeters, E., Hony, S., Van Kerckhoven, C., et al. 2002, *A&A*, **390**, 1089
 Peeters, E., Mattioda, A. L., Hudgins, D. M., & Allamandola, L. J. 2004, *ApJL*, **617**, L65
 Peeters, E., Tielens, A. G. G. M., Allamandola, L. J., & Wolfire, M. G. 2012, *ApJ*, **747**, 44
 Ricca, A., Bauschlicher, C. W., Jr., Mattioda, A. L., Boersma, C., & Allamandola, L. J. 2010, *ApJ*, **709**, 42
 Rosenberg, M. J. F., Berné, O., Boersma, C., Allamandola, L. J., & Tielens, A. G. G. M. 2011, *A&A*, **532**, A128
 Sellgren, K., Uchida, K. I., & Werner, M. W. 2007, *ApJ*, **659**, 1338
 Sellgren, K., Werner, M. W., Ingalls, J. G., et al. 2010, *ApJL*, **722**, L54
 Sheffer, Y., Wolfire, M. G., Hollenbach, D. J., Kaufman, M. J., & Cordier, M. 2011, *ApJ*, **741**, 45
 Smith, J. D. T., Armus, L., Dale, D. A., et al. 2007a, *PASP*, **119**, 1133
 Smith, J. D. T., Draine, B. T., Dale, D. A., et al. 2007b, *ApJ*, **656**, 770
 Stock, D. J., Peeters, E., Choi, W. D.-Y., & Shannon, M. J. 2014, *ApJ*, **791**, 99
 Stock, D. J., Peeters, E., Tielens, A. G. G. M., Otaguro, J. N., & Bik, A. 2013, *ApJ*, **771**, 72
 Tielens, A. G. G. M. 2005, *The Physics and Chemistry of the Interstellar Medium* (Cambridge: Cambridge Univ. Press)
 Tielens, A. G. G. M. 2008, *ARA&A*, **46**, 289
 Tielens, A. G. G. M. 2013, *RvMP*, **85**, 1021
 Treffers, R., & Cohen, M. 1974, *ApJ*, **188**, 545
 Van Kerckhoven, C. 2002, PhD thesis, Institute of Astronomy, Katholieke Univ. Leuven
 Van Kerckhoven, C., Hony, S., Peeters, E., et al. 2000, *A&A*, **357**, 1013
 Werner, M. W., Roellig, T. L., Low, F. J., et al. 2004, *ApJS*, **154**, 1